DISEASES AND DISORDERS

The pleuroparenchymal fibroelastosis atlas reveals aberrant cell states and their zonation as an alternate roadmap to lung fibrosis

Jannik Ruwisch[1,2,3]†, Aurélie Cazes[4]†, Lena M. Leiber[1,2]†, Raphaël Borie[5,6], Lavinia Neubert[2,7], Leonard Christian[1,2], Vincent Thomas de Montpréville[8], Adam Szmul[9], Farah Moussa[10], Stijn E. Verleden[11], Svenja Gaedcke[1,2], Jan Hegermann[2,12], Jan Fuge[1,2], Matthias Ballmaier[13], Jan C. Kamp[1,2,7], Mark Greer[1,2], Peter Braubach[2,7], Christopher Werlein[2,7], Fabius Ius[14], Theresa Graalmann[2,15,16], Kalil Aburahma[14], Laurens J. De Sadeleer[17,18], Ryoko Egashira[9], Maximilian Ackermann[7,19], Daisuke Yamada[9], Marius M. Hoeper[1,2], Christine Falk[2,20], Jens Gottlieb[1,2], Herbert B. Schiller[21], Bart Vanaudenaerde[17], Benjamin Seeliger[1,2], Marie-Pierre Debray[22], Jean Francois Bernaudin[23], Lars Knudsen[2,24], Emmanuel Bergot[25], Joseph Jacob[9,26], Hervé Mal[27], Danny Jonigk[7,19], Sabine Dettmer[2,28], Pierre Mordant[29], Antje Prasse[1,2,30,31], Elie Fadel[32], Wim A. Wuyts[17,18], Bruno Crestani[5,6], Naftali Kaminski[33], Aurélien Justet[10,25,33]*†, Jonas C. Schupp[1,2,30,33]*†

Pleuroparenchymal fibroelastosis (PPFE) is a progressive interstitial lung disease (ILD) with defining histology of intra-alveolar fibrosis with septal elastosis (AFE), suggesting unique cellular disease processes. Here, we present a binational single-nucleus RNA sequencing atlas of PPFE, based on explanted lungs from 40 patients. Immunofluorescence microscopy, RNA in situ hybridization, micro–computed tomography (CT), and hierarchical phase-contrast (HiP) synchrotron CT provided spatial context. We identify PPFE-associated adventitial and elastofibrotic fibroblasts as key drivers of elastotic remodeling within an inflammatory microenvironment, maintained by immune cells forming tertiary lymphoid structures. Spatial mapping reveals an intriguing zonation of AFE, maintained by intercellular circuits between PPFE-associated cell types. Comparative analysis with idiopathic pulmonary fibrosis highlights *CTHRC1*+ fibrotic fibroblasts and aberrant basaloid cells as conserved profibrotic cellular machinery mediating collagen deposition across ILDs. This integrative atlas defines the cellular landscape of PPFE and dissects elastotic from fibrotic remodeling, providing a molecular rationale for niche-specific therapeutic strategies.

INTRODUCTION

Pleuroparenchymal fibroelastosis (PPFE) represents a rapidly progressive interstitial lung disease (ILD) that predominantly affects females (*1*–*3*). Aside from lung transplantation, no specific treatment options are available for PPFE (*4*). In most cases, no identifiable cause exists and PPFE is considered idiopathic (iPPFE). PPFE can, however, occur secondary to allogenic stem cell transplantation, autoimmune conditions, or lung transplantation, the latter being incorporated within the restrictive allograft syndrome (RAS). PPFE histopathology is characterized by dense fibrosis of the visceral pleura and a distinct pattern of intra-alveolar fibrosis with septal elastosis (AFE) with deposition of elastic fibers along the residual alveolar walls and intra-alveolar deposition

[1]Clinic for Respiratory Medicine and Infectious Diseases, Hannover Medical School, Hannover, Germany. [2]Biomedical Research in End-Stage and Obstructive Lung Disease (BREATH), German Center for Lung Research (DZL), Hannover, Germany. [3]PRACTIS Clinician Scientist Program, Dean's Office for Academic Career Development, Hannover Medical School, Hannover, Germany. [4]Département de Pathologie, Hôpital Bichat-Claude Bernard, AP-HP and Université Paris Cité, INSERM U1149, CRI, Paris, France. [5]Service de Pneumologie, Allergologie et Transplantation, AP-HP, Hôpital Bichat, F-75018 Paris, France. [6]Université Paris Cité, Inserm, UMR 1149, Centre de Recherche de l'Inflammation, F-75018 Paris, France. [7]Institute of Pathology, Hannover Medical School, Hannover, Germany. [8]Institute of Pathology, Marie Lannelongue Hospital, Le Plessis-Robinson, France. [9]Satsuma Lab, Hawkes Institute, University College London, London, UK. [10]UMR 6030-ISTCT-CNRS, Normandy University, Caen, France. [11]Department of Antwerp Surgical Training, Anatomy and Research Centre, Faculty of Medicine, University of Antwerp, Wilrijk, Belgium. [12]Institute of Functional and Applied Anatomy, Research Core Unit Electron Microscopy, Hannover Medical School, Hannover, Germany. [13]Central Research Facility Cell Sorting, Hannover Medical School, Hannover, Germany. [14]Department of Cardiothoracic, Transplantation and Vascular Surgery, Hannover Medical School, Hannover, Germany. [15]Junior Research Group Translational Immunology, TWINCORE, Centre for Experimental and Clinical Infection Research, a joint venture between the Helmholtz Centre for Infection Research and the Hannover Medical School, Hannover, Germany. [16]Department for Rheumatology and Immunology, Hannover Medical School, Hannover, Germany. [17]Department of Chronic Diseases and Metabolism, KU Leuven, Leuven, Belgium. [18]Unit for Interstitial Lung Diseases, Department of Respiratory Diseases, University Hospitals Leuven, Leuven, Belgium. [19]Institute of Pathology, Aachen Medical University, RWTH, Aachen, Germany. [20]Institute of Transplant Immunology, Hannover Medical School, Hannover, Germany. [21]Institute of Lung Biology and Disease and Comprehensive Pneumology Center with the CPC-M bioArchive, Helmholtz Zentrum Muenchen, Member of the German Center for Lung Research (DZL), Munich, Germany. [22]Service de Radiologie, Hôpital Bichat, APHP; UMR Inserm 1149, CRI; FHU INFIRE, Paris, France. [23]Faculty of Medicine, Sorbonne Université, Paris, France. [24]Department of Functional and Applied Anatomy, Hannover Medical School, Hannover, Germany. [25]Department of Pulmonary Medicine, Regional ILD Expert Center, University Hospital of Caen, Caen, France. [26]UCL Respiratory, University College London, London, UK. [27]Service de Pneumologie B et Transplantation, Assistance Publique–Hôpitaux de Paris, Hôpital Bichat, Paris, France. [28]Institute of Diagnostic and Interventional Radiology, Hannover Medical School, Hannover, Germany. [29]Assistance Publique–Hôpitaux de Paris, Service de Chirurgie Thoracique, Hôpital Bichat; INSERM, Unité 1152; Université Paris Diderot, Paris, France. [30]Fraunhofer Institute for Toxicology and Experimental Medicine, Hannover, Germany. [31]Department of Biomedicine, University of Basel, Basel, Switzerland. [32]Department of Thoracic Surgery and Heart-Lung transplantation, Université Paris-Saclay, Marie Lannelongue Hospital, Le Plessis Robinson, France. [33]Section of Pulmonary, Critical Care and Sleep Medicine, Yale School of Medicine, New Haven, CT, USA.
*Corresponding author. Email: Justet-A@chu-caen.fr (A.J.); Schupp.Jonas@mh-hannover.de (J.C.P.)
†These authors contributed equally to this work.

of collagen fibrils (*1*, *5*, *6*). In addition, lymphoid cell aggregates have been frequently observed in AFE lesions (*5*).

The advent of single-cell RNA sequencing (scRNA-seq) has markedly revolutionized our understanding of biology in general (*7*–*9*) and the pathogenesis of various respiratory diseases in particular (*10*–*14*). This is especially true for idiopathic pulmonary fibrosis (IPF) (*10*, *13*), the most common ILD (*15*, *16*). IPF is characterized by a unique histological pattern called usual interstitial pneumonia (UIP) (*17*). scRNA-seq enabled identification of aberrant cell populations that form the UIP pattern of IPF including *CTHRC1*+ fibrotic fibroblasts, aberrant basaloid cells, ectopic systemic-venous endothelial cells (ECs), and *SPP1*+ profibrotic macrophages (*10*). Given this focus on UIP, non-UIP lung diseases have not been scrutinized scRNA-seq, leaving potential gaps in our knowledge.

It is currently unknown to what extent scRNA-seq findings in IPF are transferable to other fibrotic ILDs such as PPFE, given clear radiological and histological distinctions that reflect different underlying processes (*18*): PPFE typically affects nonsmoking female patients with relatively young age (*1*, *2*, *4*), whereas IPF more commonly occurs in aged male ex-smokers (*1*, *4*, *16*). PPFE usually affects the upper lobes of the lungs, contrasting IPF remodeling, predominating in the lower lobes. Histopathologically, UIP is characterized by spatiotemporal heterogeneous fibrosis, destruction of the lung architecture, and bronchiolization of the distal lung (*17*), whereas AFE is a homogeneous fibrosis with preserved lung scaffolds and global lung architecture (*5*, *6*).

Given these substantial differences between PPFE and IPF, it remains unknown if PPFE is composed of the usual IPF-associated pathological cell types or if PPFE-specific cell populations exist. Equally, an understanding of any shared disease-spanning principles of lung fibrosis within these two prototypically progressive but clinically divergent ILDs would be important. Last, PPFE research has lacked a compass to guide which cellular or molecular targets would be useful to test in clinical trials. Closing these knowledge gaps is essential to develop ILD-spanning treatment approaches and for providing a rationale for PPFE-specific treatment approaches.

Here, we set up the international collaborative single cell–resolved PPFE atlas. Following integration with a recently published IPF dataset (GSE286182) (*19*), we capture the cellular landscape of these progressively fibrotic ILDs. For validation and localization purposes, we use micro–computed tomography (CT) guided multiplex RNA in situ hybridization (ISH), immunofluorescence (IF) microscopy, hierarchical phase-contrast (HiP) synchrotron CT (*20*), and transmission electron microscopy (TEM) and complement these with extensive in silico ligand-receptor analysis.

RESULTS

Cohort and dataset characteristics

Biobanked lung tissue from 40 patients with PPFE undergoing lung transplantation in three European ILD and transplant centers [one in Hannover, Germany (PPFE-GER; $n = 23$) and two in Paris, France (PPFE-FR; $n = 17$)] as well as 16 controls (Fig. 1A and Table 1) were analyzed. PPFE diagnosis was confirmed on the basis of high-resolution computed tomography (HRCT) and typical histopathology (Fig. 1, B and C) in multidisciplinary team discussions (Table 1 and figs. S1 and S2). Female patients were more prevalent in both PPFE cohorts (*21*, *22*) (PPFE-GER: 65.2%; PPFE-FR: 52.9%; Table 1) as in the German control cohort (CTRL-GER: 37.5%). The median age at diagnosis was 41.3 years (Q1 = 29.3 years; Q3 = 50.8 years; Table 1), whereas prevalence of tobacco smoking was limited to 15% in the PPFE cohort. In contrast, the median age of CTRL-GER population [61.4 years (Q1 = 53.5 years; Q3 = 66.9 years)] was higher in the CTRL population (Pval < 0.001). CTRL specimens ($n = 16$) were equally derived from two sources: eight samples from lung downsizing during transplantation and eight samples from peripheral tumor resections (Table 1). Smoking status significantly differed between PPFE and CTRL cohorts, with a higher proportion of current or former smokers among CTRL subjects (Pval < 0.001; Table 1).

Our PPFE cohorts are therefore dominated by young, nonsmoking and female patients, contrasting published IPF scRNA-seq datasets, which consist mainly of older, male ex-smokers (*10*, *13*). The etiology of PPFE was considered idiopathic in most cases, despite extensive diagnostic workup (PPFE-GER: 87.0%; PPFE-FR: 82.4%; Table 1).

In total, 320,541 single-nucleus transcriptomes were profiled. We integrated our dataset with 199,379 nuclei sampled from explant tissue of nine patients with IPF from Leuven, Belgium (Fig. 1A) [GSE286182 (*19*)]. All major cell types of the human lung were identified across diseases and subjects based on distinct marker gene expression (Fig. 1, D to F; fig. S3A; and tables S4 and S5),

Cell frequency analysis by lineage demonstrated marked shifts toward the lymphoid cell lineage in the PPFE cohorts (Fig. 1, G and H). Moreover, lymphoid cell frequencies exhibited some variation among PPFE-GER and PPFE-FR, which correlated significantly with the proportion of remodeled parenchyma in serially sectioned Elastica van Gieson (EvG) or orcein-stained specimens (Pearson's $R = 0.43$; Pval = 0.006; fig. S3, B and C). Fractions of remodeled parenchyma were higher in PPFE-GER compared to PPFE-FR (Fig. 1G).

Detailed descriptive statistics of cell types and lineages per disease are provided in the Supplementary Materials, with selected conspicuities highlighted below. Raw sequencing data of the PPFE atlas were deposited on the Gene Expression Omnibus under GSE301982 (https://ncbi.nlm.nih.gov/geo/query/acc.cgi?acc=GSE301982), and processed data can be explored on the PPFE atlas web page (PPFEatlas.com).

Mesenchymal diversity in PPFE

Mesenchymal cells constituted 20.8% of all profiled cells (Fig. 2A). Within this subset (Fig. 2, B to D), we identified resident alveolar fibroblasts (*LMCH1* and *FRAS1*), subpleural fibroblasts (*HAS1* and *WT1*), adventitial fibroblasts (*MFAP5*, *PI16*, and *SCARA5*), and airway fibroblasts (*WNT5A* and *COL10A1*; Fig. 2E and tables S6 to S8). In addition, pericytes (*COXI2*) and smooth muscle cells (*DES* and *MYH11*) were abundant throughout all cohorts. Within the PPFE cohorts, mesenchymal cells were the main contributors to collagen and elastic fiber deposition: *CTHRC1*+ fibrotic fibroblasts—the major profibrotic cell type in IPF (*10*, *23*) with high expression of collagen synthesis–related genes (*COL1A1* and *COL1A2*; Fig. 2E)—occurred not only in IPF (9.18 ± 4.11%, adj.Pval$_{vs.CTRL}$ < 0.001) but also, to a similar extent, in PPFE (PPFE-GER: 9.18 ± 3.46%, adj.Pval$_{vs.CTRL}$ < 0.001 and PPFE-FR: 9.19 ± 3.83% adj.Pval$_{vs.CTRL}$ < 0.001; Fig. 2F and table S7). Single-sample gene set enrichment analysis (ssGSEA) for matrisomeDB (*24*)–related extracellular matrix (ECM) domains confirmed *CTHRC1*+ fibrotic fibroblasts as the main source of parenchymal collagen and proteoglycans such as *DCN*, *BGN*, and *LUM* in the PPFE lung (Fig. 2, E and G).

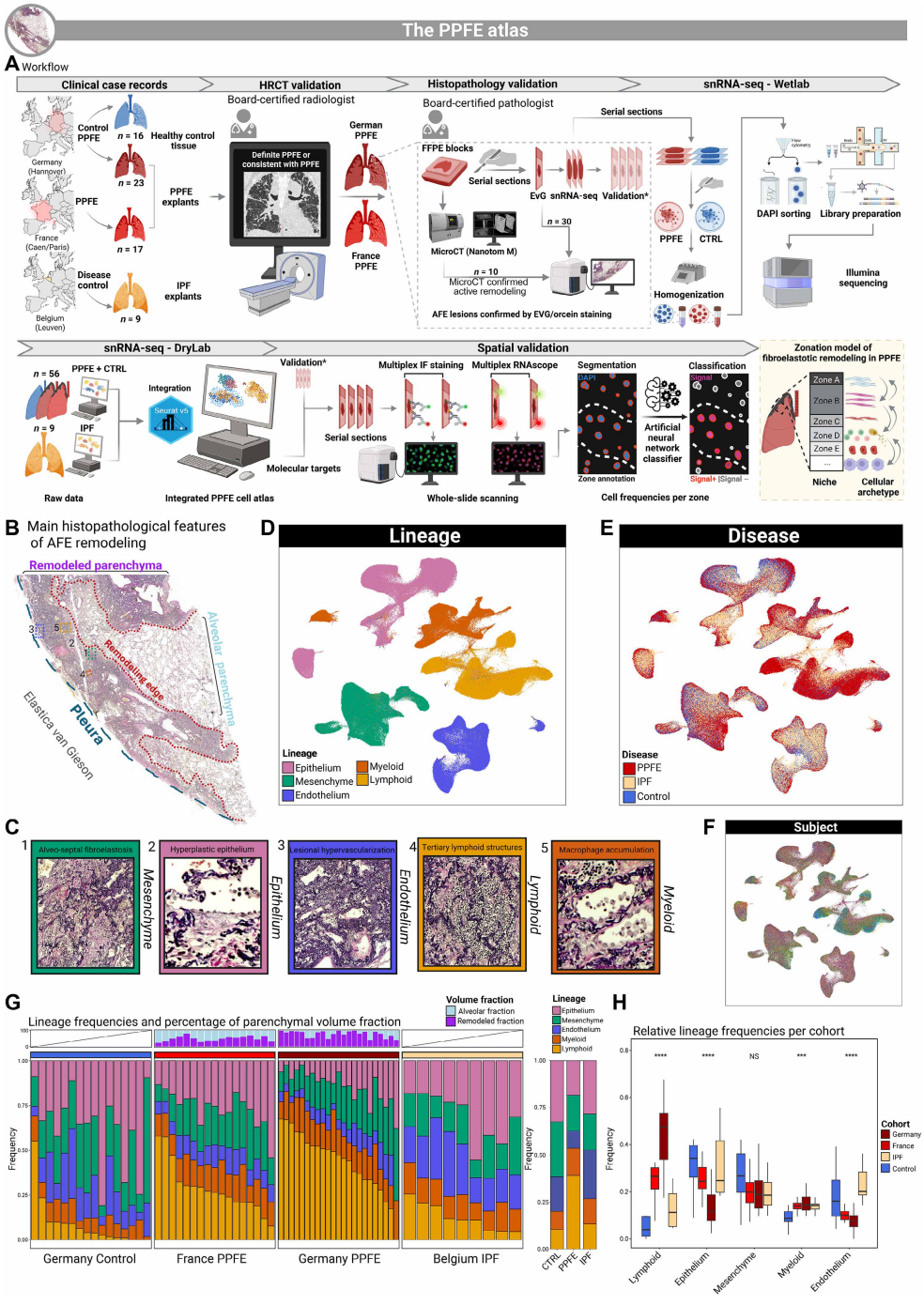

Fig. 1. Experimental design and analysis of lineage composition. (**A**) Lung tissue from 23 German and 17 French patients was used to construct the 320,541 single nuclei spanning the PPFE atlas, whereas published snRNA-seq data of 199,379 nuclei from nine patients with IPF (GSE286182) served as disease control. One FFPE block per PPFE and per CTRL lung was serially sectioned. Initial 50-µm-thick sections were used for nuclei isolation, whereas subsequent 5-µm sections served for validation via IF staining or RNA ISH. Automated whole-slide cell segmentation in conjunction with ANN algorithm-based cell classification for marker gene positivity was used for spatial niche profiling. (**B**) EvG-stained PPFE slides can be segmented into remodeled (purple) and unremodeled alveolar parenchyma (light blue). Both zones are demarcated by a sharp line referred to as (fibroelastotic) remodeling edge. (**C**) Within the remodeled parenchyma, PPFE lesions typically consist of subpleural eosinophilic fibrosis and adjacent areas of AFE. Colored boxes highlight lineage-related histopathological hallmarks of AFE remodeling. (**D**) Uniform Manifold Approximation and Projection (UMAP) representation of 519,920 nuclei, color coded according to lineage. (**E**) UMAP by disease. (**F**) UMAP by subject. (**G**) Stacked bar plots of relative lineage frequencies per subject colored by lineage and split by cohort. Subjects were ordered after frequencies of lymphoid cells (bottom). Surface fractions were calculated for remodeled (light blue) and unremodeled (purple) tissue segmented on serially sectioned EvG-stained images as exemplified in [(B), top]. (**H**) Relative cell frequencies were calculated as average per subject and are presented as box plots. Intercohort statistics were assessed on the subject level under the use of the Wilcoxon rank sum test. Created in BioRender. Schupp, J. (2026) https://biorender.com/br8cgh6. Panels (B) and (C) contain representative PPFE lesions that are shown elsewhere in the manuscript.

Table 1. Detailed PPFE and CTRL cohort statistics. Statistical tests were conducted for given probabilities. None of the investigated variates reached statistical significance across PPFE cohorts, whereas comparisons of smoking status and age reached statistical significance when testing across PPFE and CTRL cohorts. DLCO, diffusion capacity of the lungs for carbon monoxide; FVC, forced vital capacity; LTX, lung transplanation.

	FRENCH PPFE (*N* = 17)	GERMAN PPFE (*N* = 23)	Total PPFE (*N* = 40)	*P* value (French vs German PPFE)	CTRL (*N* = 16)	*P* value (French vs. German PPFE vs. CTRL)
Sex *N* (%)				0.433*		0.232*
Female	9 (52.9%)	15 (65.2%)	24 (60.0%)		6 (37.5%)	
Male	8 (47.1%)	8 (34.8%)	16 (40.0%)		10 (62.5%)	
Smoking status				0.165*		<0.001*
No	16 (94.1%)	18 (78.3%)	34 (85.0%)		3 (18.8%)	
Former	1 (5.9%)	5 (21.7%)	6 (15.0%)		5 (31.2%)	
Active	0	0	0		1 (6.2%)	
Either active/ former#	0	0	0		5 (31.2%)	
Unknown	0	0	0		2 (12.5%)	
Age at diagnosis (years)				0.940†		<0.001†
Median (Q1, Q3)	42.0 (29.5, 51.0)	41.2 (29.9, 50.1)	41.3 (29.3, 50.8)		61.4 (53.5, 66.9)	
Main CT pattern *N* (%)				0.343‡§		
Definite or consistent with PPFE	17 (100.0%)	23 (100.0%)	40 (100.0%)			
Concomitant CT patterns *N* (%)				0.111*		
Emphysema	0 (0.0%)	1 (4.3%)	1 (2.5%)			
Indeterminate	2 (11.8%)	0 (0.0%)	2 (5.0%)			
None	8 (47.1%)	17 (73.9%)	25 (62.5%)			
NSIP	2 (11.8%)	0 (0.0%)	2 (5.0%)			
UIP	5 (29.4%)	5 (21.7%)	10 (25.0%)			
Main histology pattern				0.343‡¶		<0.001*
Definite or consistent with PPFE	17 (100.0%)	23 (100.0%)	40 (100.0%)		0	
Tumor resection	0	0	0		8 (50%)	
Downsizing lung	0	0	0		8 (50%)	
Concomitant histology patterns *N* (%)				0.415*		
Bronchiolitis	1 (5.9%)	0 (0.0%)	1 (2.5%)			
Emphysema	0 (0.0%)	1 (4.3%)	1 (2.5%)			
Granuloma	1 (5.9%)	1 (4.3%)	2 (5.0%)			
NSIP	3 (17.6%)	4 (17.4%)	7 (17.5%)			
UIP	2 (11.8%)	8 (34.8%)	10 (25.0%)			
PPFE subtype				0.687*		
Idiopathic	14 (82.4%)	20 (87.0%)	34 (85.0%)			
Secondary	3 (17.6%)	3 (13.0%)	6 (15.0%)			
Last FVC before LTX (% predicted)				0.451†		
Median (Q1, Q3)	34.0 (24.0, 40.0)	30.0 (20.0, 37.5)	32.0 (22.8, 38.3)			
Last DLCO before LTX (% predicted)				0.606†		
Median (Q1, Q3)	35.0 (31.5, 37.0)	29.0 (25.0, 33.0)	35.0 (28.5, 37.0)			
History of antifibrotics *N* (%)				0.093*		
Nintedanib	1 (6.2%)	2 (8.7%)	3 (7.7%)			
Pirfenidone	1 (6.2%)	2 (8.7%)	3 (7.7%)			

*Pearson's chi-square test. †Kruskal-Wallis rank sum test. ‡Chi-square test. §HRCT patterns were validated by board-certified radiologists at each study site. ¶Histopathology patterns were reviewed by board-certified pathologists at each study site. #Temporal extent of nicotine abuse was not available for donors of downsizing lungs.

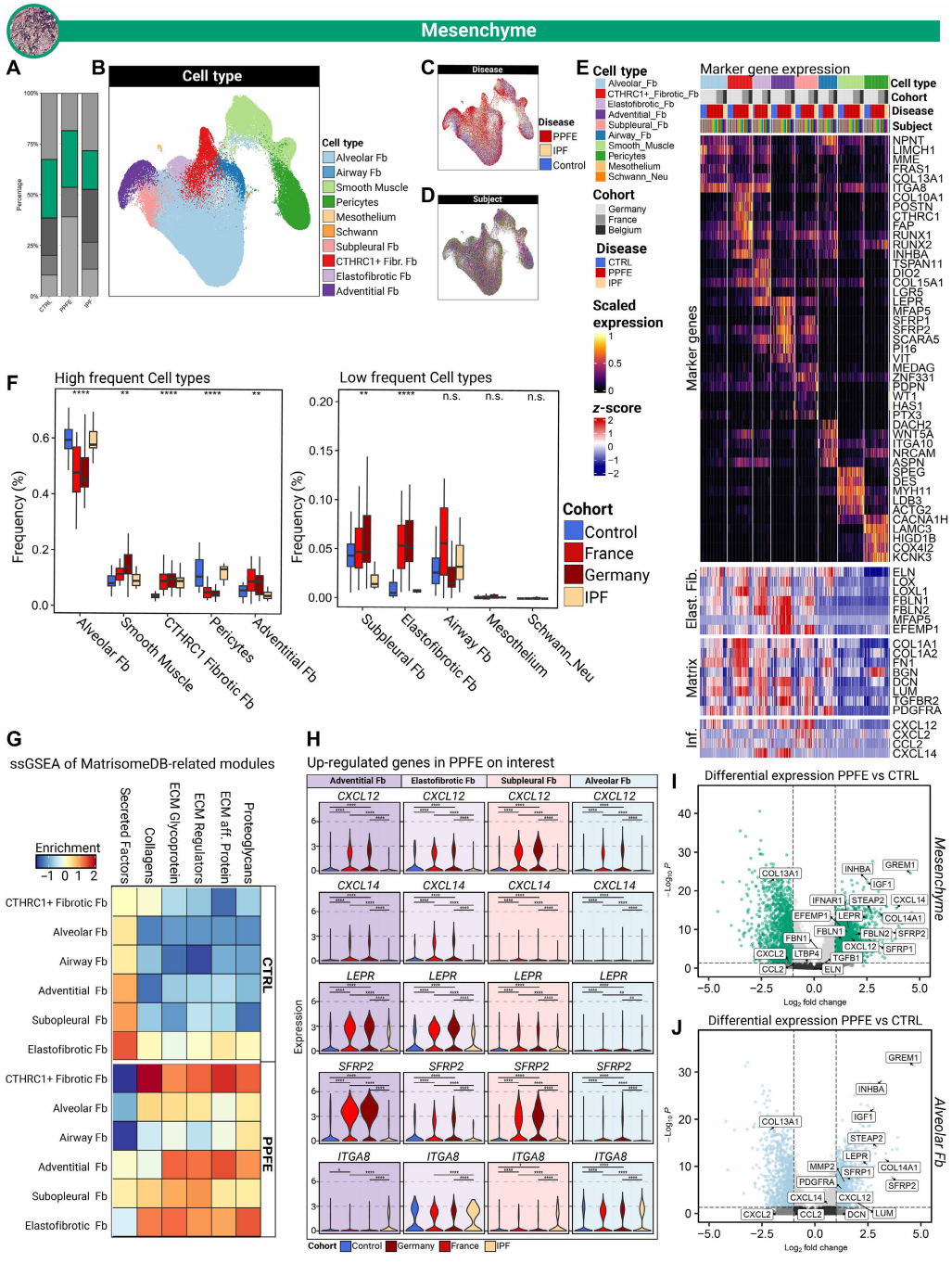

Fig. 2. Mesenchymal archetypes in the PPFE lung. (**A**) Relative fraction of mesenchymal nuclei. (**B**) UMAP of identified fibroblast (Fb) subsets and other cell types within the mesenchymal lineage. (**C**) UMAP by disease. (**D**) UMAP by subject. (**E**) Unity-scaled average expression of canonical markers per subject (top heatmap). Subjects were grouped after cohort and disease. Each subject was assigned to a unique color. Genes related to elastic fiber formation, ECM remodeling, and inflammatory signaling were *z*-score normalized per average expression per cell type and subject and plotted across cohorts and disease (bottom heatmap). (**F**) Box plots display the relative distribution of each mesenchymal cell type relative to the total mesenchymal lineage compartment, stratified by disease-related cohort. n.s., not significant. Whiskers indicate 1.5 times the interquartile range (IQR). Statistical comparisons across cohorts were performed using the Kruskal-Wallis test. Post hoc tests were performed under the use of the Wilcoxon rank sum test, with Bonferroni correction for multiple comparisons across cohorts and cell types. Detailed results are provided in table S7. (**G**) ssGSEA for MatrisomeDB-curated ECM gene modules in mesenchymal cell types. (**H**) Differential gene expression of selected genes. (**I**) Volcano plot of DESeq2 differential expression following subject-level pseudobulk aggregation of alveolar fibroblasts comparing PPFE and CTRL, with *P* values adjusted for multiple testing by the Benjamin-Hochberg method. Genes exceeding $\log_2$FC (fold change) > 1 and adj. *P*val < 0.05 were colored in green. Supervised gene annotation highlights genes related to remodeling in PPFE. (**J**) Volcano plot of DESeq2 differential expression following subject-level pseudobulk aggregation of alveolar fibroblasts comparing PPFE and CTRL, with *P* values adjusted for multiple testing by the Benjamin-Hochberg method. Genes exceeding $\log_2$FC > 1 and adj. *P*val < 0.05 were colored in light blue. Gene annotation was performed in a supervised manner, highlighting genes related to remodeling in PPFE.

The two major PPFE-specific intramesenchymal shifts were noted, however, for adventitial fibroblasts (PPFE-FR: 9.04 ± 5.15%, adj.Pval$_{vs.CTRL}$ = 0.023 and PPFE-GER: 8.19 ± 4.19%, adj.Pval$_{vs.CTRL}$ = 0.024) and adventitial-like "elastofibrotic" fibroblasts (*25*) (Fig. 2F and tables S7 to S9). The latter received their name due to their transcriptional overlap with adventitial fibroblasts (*SFRP2*, *SCARA5*, and *PI16*) and *CTHRC1*+ fibrotic fibroblasts (*INHBA*, *FN1*, and *ASPN*; Fig. 2E). In addition, elastofibrotic fibroblasts coexpressed elastic fiber formation–related genes such as (*ELN*, *LOXL1*, *FBLN1*, and *FBLN2*; Fig. 2E) as well as *LEPR* and the alveolar fibroblast marker *ITGA8* (Fig. 2H) (*26*, *27*). Meanwhile, they lack expression of the adventitial fibroblast marker *MFAP5* (Fig. 2E). *LEPR* expression was up-regulated in PPFE mesenchyme versus CTRL and IPF in general and was particularly highly expressed in elastofibrotic fibroblasts (Fig. 2, H and I, and tables S10 and S11). This marker emphasizes the elastotic-to-profibrotic fate plasticity of elastofibrotic fibroblasts as murine *Lepr*+ fibroblasts represent the major precursor population of *Cthcr1*+ fibrotic fibroblasts in mice (*26*). Additional discriminating marker genes of elastofibrotic fibroblasts included *DIO2* and *COL15A1* and lipid metabolism–related genes such as *APOD* or *STEAP2* (Fig. 2E and tables S8 and S9).

Notably, PPFE alveolar fibroblasts demonstrated a significantly increased expression of *GREM1* and *IGF1* as well as the adventitial collagen *COL14A1*, potentially illustrating an early phenotypic shift from resident alveolar cell populations to mesenchymal cellular archetypes physiologically located in the loose connective tissue of the interlobar septum, bronchovascular bundle, or the subpleural connective tissue (Fig. 2J and table S12) (*11*).

Inflammatory activation states of fibroblasts in PPFE

Intramesenchymal differential expression analysis between PPFE and CTRL uncovered up-regulation of a gene battery characteristic for the recently described mesenchymal cell state termed "inflammatory fibroblasts" (*28*) including *CXCL12* and *CXCL14* (Fig. 2H) as well as interferon signaling-related genes such as *IFNAR1* (Fig. 2I). In murine bleomycin-induced lung fibrosis, *Cxcl12*+ inflammatory fibroblasts arise from alveolar fibroblasts and differentiate into *CTRHC1*+ fibrotic fibroblasts (*27*) while localizing to sites of fibrotic remodeling in IPF (*27*). In PPFE, multiple fibroblast subsets including subpleural, adventitial, and elastofibrotic fibroblasts acquire this inflammatory activation state as highlighted by the expression of *CXCL12*. Notably, we observed a higher expression of these cytokines in PPFE fibroblasts compared to CTRL and IPF (Fig. 2H). However, the details of the inflammatory activation vary: *HAS1*+*WT1*+ subpleural fibroblasts exclusively expressed an interferon/TNF (tumor necrosis factor) response signature with coexpression of *CXCL12*, *CXCL2*, and *CCL2* (Fig. 2E). Coexpression of *CXCL12* and *CXCL14* was restricted to *LEPR*+*ITGA8*+*DIO2*+ elastofibrotic fibroblasts and *SFRP2*+ adventitial fibroblasts (Fig. 2H). In contrast to PPFE, *CXCL14* and *CXCL12* expression in mesenchymal cells from IPF or CTRL samples was almost absent (Fig. 2H).

Immune cell landscape in PPFE

In line with the increased expression of the aforementioned lymphocyte chemoattractant *CXCL12*, we observed a significant increase in relative cell frequency of lymphoid cell proportions in PPFE against CTRL and IPF, a finding that was replicated in both PPFE cohorts (PPFE-GER: 43.7 ± 16.9%; PPFE-FR: 28.7 ± 13.9%; CTRL: 8.52 ± 13.76%; IPF: 12.6 ± 7.6%; adj.Pval$_{vs.CTRL}$ < 0.01 and adj.Pval$_{vs.CTRL}$ < 0.01; adj.Pval$_{vs.IPF}$ < 0.01 and adj.Pval$_{vs.IPF}$ = 0.02; Fig. 1, G and H, and tables S4 and S5). Phenotyping of lymphoid cells revealed a broad repertoire of immune cells emerging in the PPFE lung (Fig. 3, A and B, and tables S13 to S16), further explored in the Supplementary Materials (fig. S4). By contrast, lymphoid cell frequencies were not increased in IPF (Fig. 1H, adj.Pval$_{vs.CTRL}$ = 0.75, and table S5).

Myeloid immune cell populations demonstrated a relative decrease in alveolar macrophages (AMs) (PPFE-GER: 1.83 ± 2.69%, adj.Pval$_{vs.CTRL}$ < 0.001; PPFE-FR: 1.57 ± 0.96%, adj.Pval$_{vs.CTRL}$ < 0.001; Fig. 3C, fig. S4, and tables S17 to S19). The AM frequency was not increased within the IPF dataset, with 22.56% of myeloid cells being identified as AMs (adj.Pval$_{vs.CTRL}$ = 1). Further differences in cell frequencies between PPFE and IPF included increased proportions of classical monocytes within the lung tissue in PPFE (cMono; adj.Pval$_{vs.CTRL}$ each < 0.001). Fractions of *SPP1*+*CHIT1*+ profibrotic macrophages were not elevated in the PPFE lung (adj.Pval$_{vs.CTRL}$ = 1).

Immunomesenchymal cell communication networks partition into three distinct niches

Correlation of in silico cellular cross-talk analysis with in situ mapping of lymphoid and myeloid cell types indicated three intercellular signaling hubs in PPFE lesions:

We observed an enhanced signaling circuit centered around inflammatory fibroblast populations and lymphocytes forming tertiary lymphoid structures (TLSs: noncapsulated organized lymphoid cell aggregates in nonlymphoid tissues) (*29*, *30*) (Fig. 3D). Within this TLS niche, *SFRP2*+ adventitial and elastofibrotic fibroblasts colocalized with CD4+ and CD20+ positive lymphocytes (Fig. 3D). Ligand-receptor analyses highlighted signaling between *CXCL12*+ fibroblast and lymphocyte subsets expressing the corresponding receptor *CXCR4* as a prominent non-ECM–related pathway. Expression of *CXCL12* was increased in multiple fibroblast populations (Fig. 2H). ISH confirmed *CXCL12* expression within the TLS niche (Fig. 3, E to G). *CXCR4* was up-regulated in lymphocyte subpopulations (Fig. 3, H and I). Together, this suggests the *CXCL12-CXCR4* axis as a potential link between recruited immune cells and inflammatory fibroblasts in PPFE.

Targeted exploration of TLS formation–related cell types identified a *BCL6*+*ICOS*+*PDCD1*+ and *CXCR5*+ population of T follicular helper cells within the cluster of CD4+ effector memory T cells with increased expression of *CXCL13* in both PPFE cohorts (Fig. 3, H and I). In addition, we observed potential *RORC*-expressing lymphoid TLS inducer cell populations such as T helper 17 (T_H17) cells alongside a minor population of ILC3 (Fig. 3H and table S16). In particular, T_H17 cells were abundant in the PPFE lungs and, to a significantly lesser extent, in IPF lungs (Fig. 3A, adj.Pval$_{vs.IPF}$ < 0.001).

CD14+ monocytes that accumulated in the circumference of TLSs exhibited an increased cross-talk weight from diverse fibroblast subsets (peri-TLS myeloid niche; Fig. 3, J to L). Ligand-receptor analysis of the peri-TLS myeloid niche exhibited increased signaling weights between myeloid cells and adventitial, elastofibrotic, subpleural, and *CTHRC1*+ fibrotic fibroblasts (Fig. 3J). Of special interest is the fibroblast-to-monocyte communication through *CSF1-CSFR*, central for recruitment of classical and nonclassical monocytes (Fig. 3K). IF staining localized aggregates of large CD68+ macrophages within alveoli at the remodeling edge (Fig. 3L). Smaller CD14+CD68+ monocytes formed clusters in the periphery of TLSs near surrounding CD8+ T cells (Fig. 3L). Serial sections for ISH indicated peri-TLS monocytes congregating in the same topographic region as *SFRP2*+ fibroblasts, again suggesting an additive role for the predicted fibromyeloid cross-talk in TLS formation of PPFE.

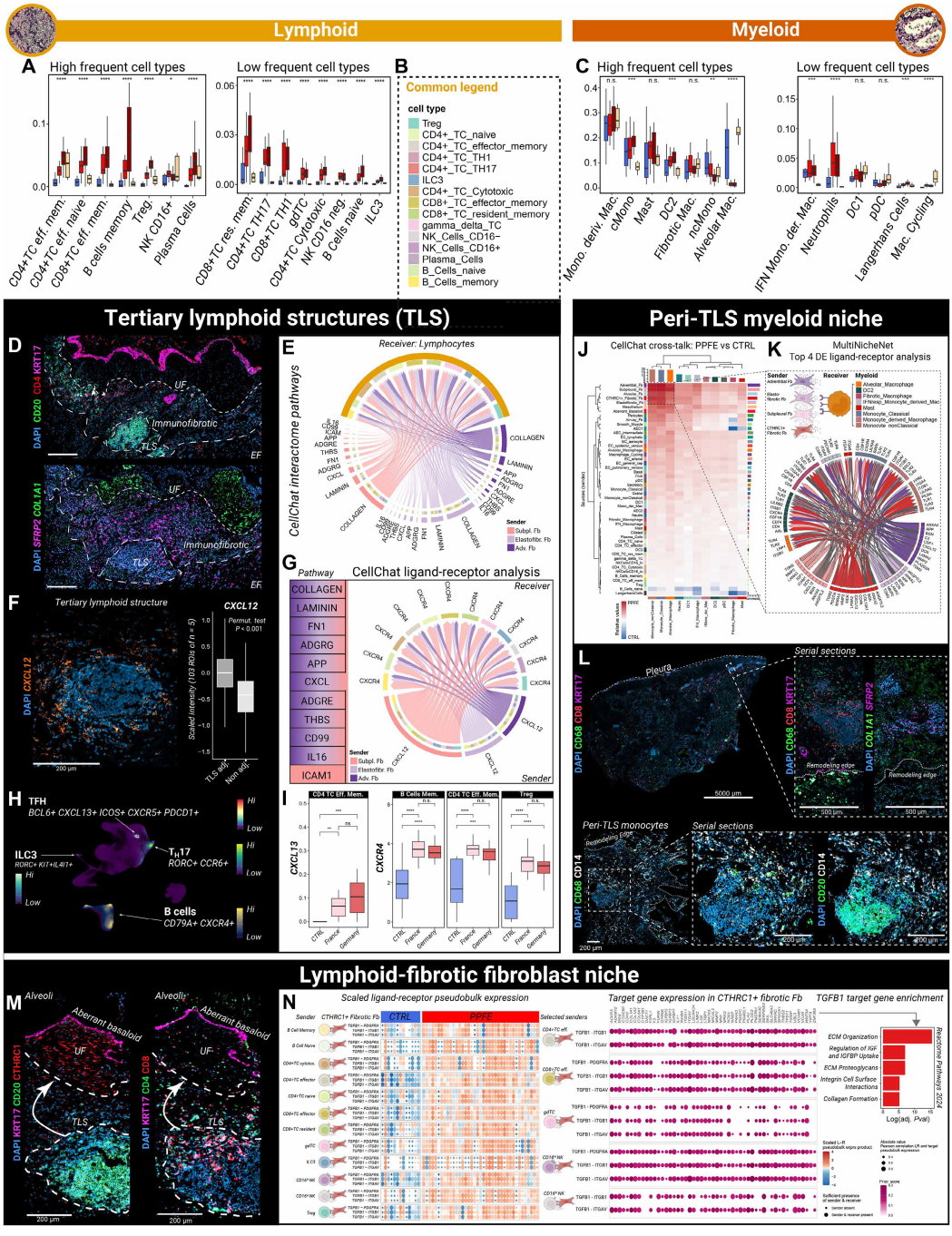

Fig. 3. Immune cell repertoire and immunofibrotic cross-talk in PPFE. (**A**) Frequencies of each lymphoid cell type relative to all nuclei from all lineages per sample. Statistical comparisons across cohorts was performed using the Kruskal-Wallis test. Detailed results are provided in table S14. (**B**) Common legend of lymphoid cell types. (**C**) Relative distribution of each myeloid cell type relative to the total myeloid lineage compartment. Detailed results are provided in table S18. (**D**) TLS niche. Representative serial IF and ISH staining of neighboring immune cells and fibroblasts (Fb). UF, usual fibrotic niche; EF, elastofibrosis zone. (**E**) Intercellular pathway analysis between subpleural fibroblasts, adventitial fibroblasts, elastofibrotic fibroblasts (sender), and lymphoid cell subsets (receiver). (**F**) Representative ISH of the *CXCL12* expression in the peri-TLS niche and spatial enrichment analysis of the scaled *CXCL12* intensity across ROIs adjacent ($n = 52$ ROIs) and nonadjacent ($n = 51$ ROIs) to TLSs. Scale bar, 200 μm. (**G**) Predicted interaction of subpleural, adventitial, and elastofibrotic fibroblasts (sender) and lymphoid subsets (receiver). Chord thickness corresponds to the interaction strength (CellChatv2) for each ligand-receptor pair per cell type pair. (**H**) Nebulosa plots of TLS-related cell types. Separate nebulosa plots are in fig. S4. (**I**) Average per subject expression of TLS formation–related genes analyzed by the Wilcoxon rank sum test. (**J**) Peri-TLS niche. Comparative relative cross-talk weight analysis between PPFE and CTRL toward myeloid cells. (**K**) Chord diagram of the differential ligand-receptor analysis (PPFE versus CTRL) of top sending cell types and myeloid cells using MultiNicheNetR. (**L**) Representative IF staining of CD14- and CD68-expressing monocytes across remodeling niches in PPFE. (**M**) Lymphoid fibrotic fibroblast niche. Representative IF of the TLS in proximity to UF. Scale bars, 200 μm. (**N**) MultiNicheNetR differential ligand-receptor analysis between PPFE and CTRL focused on lymphoid-to-*CTHRC1*+ fibrotic fibroblast signaling. Created in BioRender. Schupp, J. (2026) https://biorender.com/br8cgh6.

Last, we found a profibrotic lymphofibroblastic cross-talk in accordance with the frequently observed spatial proximity of TLSs to the usual fibrotic niche composed of *CTHRC1*+ fibrotic fibroblasts and aberrant basaloid cells (further expanded on below; Fig. 3M). Targeted ligand-receptor analysis revealed uniform up-regulation of classical *TGFB1* signaling within some of the lymphoid cell subsets in the PPFE cohorts (Fig. 3N and table S20). Significantly enriched pathways included ECM remodeling and collagen synthesis (table S21). Together, these findings suggest that local immune cells may catalyze local profibrotic mesenchymal activation and fibrotic remodeling via *TGFB1* signaling.

PPFE remodeling is spatially organized into four distinct zones

Spatial in situ mapping of mesenchymal marker genes revealed a spatially organized disease pattern in PPFE, defining four niches with distinct cellular composition (Fig. 4A). From the pleural surface to apparently unremodeled alveolar parenchyma, these zones comprised (A) a "subpleural fibrosis zone," (B) a zone marked by septal elastosis and intra-alveolar collagen deposition referred to as "elastofibrosis zone," (C) an "immunofibrotic zone," and (D) a continuous band of *CTRHC1*+ fibrotic fibroblasts overlined by a monolayer of aberrant basaloid cells at the fibroalveolar remodeling edge.

In the subpleural fibrosis zone, *HAS1*+*WT1*+ subpleural fibroblasts (Fig. 4, B and C) (*13*) were identified and localized to a narrow area adjacent to the likewise *HAS1*+ mesothelium (Fig. 5, A to C). On hematoxylin and eosin and EvG stains, this area corresponded to highly eosinophilic regions with low cellularity and abundant ECM deposition (Fig. 4A). Subpleural fibroblast displayed a strong inflammatory signature with expression of interferon response genes such as *CXCL2* and *CCL2* as well as *CXCL12* and *TNFRSF12A* (Fig. 4C). In addition, enrichment analysis attributed subpleural fibroblasts with interleukin-4 (IL-4) and IL-13 signaling (Fig. 4I and table S22). The extent of this zone varied highly among patients in both cohorts and seemed to only serve as a poor indicator of the overall affected tissue within the specimen (fig. S2).

Notably, we occasionally observed TLSs in the subpleural fibrosis zone. *CXCL12* chemotaxis is sufficient to induce TLS formation (*31*), and *CXCL12*+ inflammatory cancer-associated fibroblasts colocalized with TLSs in the fibrotic tumor environment (*32*). On the single-cell level, this is paralleled by the high expression of *CXCL12* expression in *HAS1*+ subpleural fibroblasts (Fig. 2H and fig. S6).

Below, in the elastofibrosis zone, we located *SFRP2*+ adventitial (Fig. 4, D and E) and elastofibrotic fibroblasts (Fig. 4, D and F) alongside with remnants of remodeled alveolar septa and within them (Fig. 5, A, E, and F). RNA ISH coupled with phase-contrast microscopy (PCM) located *SFRP2*+ fibroblasts in close proximity to deposited elastic fibers within established AFE lesions and in thickened alveolar septa next to AFE lesions (Fig. 5G). Further characterization of PPFE-enriched adventitial fibroblasts by differentially expressed gene enrichment analysis identified five clusters of pathways (fig. S5, A and B, and table S23): Cluster C1 comprised ECM-related genes involved in elastic fiber metabolism (*EFEMP1*, *FBLN2*, *FBLN1*, and *MFAP5*) and collagens (*COL4A4*, *COL15A1*, and *COL14A1*; fig. S5B), whereas cluster C3 depicted an induction of glycosaminoglycan metabolism (fig. S5A). Meanwhile, the same enrichment analysis in elastofibrotic fibroblasts identified Reactome term clusters related to elastic fiber formation (cluster C4) but also collagen synthesis (cluster C1) and proteoglycan formation (cluster C2; fig. S5C and table S24).

Micro-CT guided ultrastructural analysis of thickened alveolar septa illustrated expanded interstitial collagen deposition and elastic fiber formation (Fig. 5L). Unexpectedly, expansion of the interstitium correlated with a continuous phenotypic alteration of the overlining alveolar epithelium with loss of lamellar bodies and increasing thickening of the interposed basal lamina on correlative ultrastructural examination (Fig. 5L).

The immunofibrotic zone (Fig. 5, I and J), an organized band of immune cell infiltrates, separates the elastofibrosis zone from the usual fibrotic niche (Fig. 5K). The relative extent of this immune cell layer was well conserved among all histologically investigated PPFE specimens ($n = 11$; Fig. 5M). Semisupervised cell quantification revealed the highest densities for CD4+ and CD8+ lymphocytes in this zone in concordance with frequently observed TLSs composed of CD4+, CD8+, and CD20+ lymphocytes (Fig. 5, A, I, and N). Furthermore, afferent and efferent vasculature from which immune cells are recruited are involved in TLS formation (*29*, *30*). Inflammatory *SFRP2*+ fibroblasts were most abundant in the immunofibrotic zone as well (Fig. 5O). This was paralleled by local enrichment of *CXCL12* expression in lesional cells adjacent to TLSs (Figs. 3F and 5J), highlighting the local immunomesenchymal cross-talk. We noted a gradual accumulation of *SFRP2*+ fibroblasts from the pleural surface toward the immunofibrotic zone (Fig. 5O). This is contrasted by the significantly lower densities of CD4+ T cells and *SFRP2*+ fibroblasts in the elastofibrosis zone, reflective of a postremodeling state. However, the extent of segmented TLSs correlated on sample level with the absolute extent of the elastofibrosis zone (Pearson's $R = 0.899$; $P\text{val} = 0.006$; fig. S7), suggesting a mechanistic link between manifested TLSs and elapsed elastofibrotic remodeling.

In direct contact with the underlying edge of alveolar-to-elastofibrotic remodeling, we identified *CTHRC1*+ fibrotic fibroblasts (Fig. 4, G and H) embedded in the immature basophilic ECM (Fig. 4A and fig. S2). Deposition of immature collagen, lack of elastic fibers in the EvG stain (Fig. 4A), and the presence of fibrotic fibroblasts in this zone (Fig. 5K) are hallmark histopathological characteristics otherwise found in fibroblastic foci of IPF lungs (*17*, *23*, *33*–*36*). Within this zone, the strong spatial expression of *COL1A1* was paralleled by IF detection of CTHRC1 (Fig. 5K), confirming *COL1A1*^{hi} cells as *CTHRC1*+ fibrotic fibroblasts. Histological quantification of *COL1A1*^{hi} cells expectedly demonstrated the highest densities in the usual fibrotic niche (Fig. 5O). Some *COL1A1*^{hi} cells exhibited coexpression of *SFRP2*. Topographically, these *SFRP2*+*COL1A1*^{hi} cells were mainly restricted to the immunofibrotic zone and the usual fibrotic niche (Fig. 5O). As *CXCL14* expression was also observed in mesenchymal cells located in the usual fibrotic niche (Fig. 5D), *CXCL14*-expressing *LEPR*+*ITGA8*+*DIO2*+ elastofibrotic fibroblasts, identified on the single-cell level, may reflect this *SFRP2*+*COL1A1*^{hi} intermediate mesenchymal state that can differentiate in *CTHRC1*+ fibrotic fibroblasts. In line, *CXCL14*+ inflammatory fibroblasts have been observed on the interstitial side of fibroblastic foci in IPF (*27*). Accordingly, ssGSEA suggested a fibrotic activation state with induced collagen synthesis in elastofibrotic fibroblasts (Fig. 2I). Last, the usual fibrotic niche was spatially restricted to a cuboidal-shaped layer of KRT17+ aberrant basaloid cells continuously overlined by *CTHRC1*+ fibrotic fibroblasts, resulting in a sharp demarcation line between the remodeled fibrotic tissue and the alveolar parenchyma (Fig. 5K). This zone will be further explored in the next paragraph.

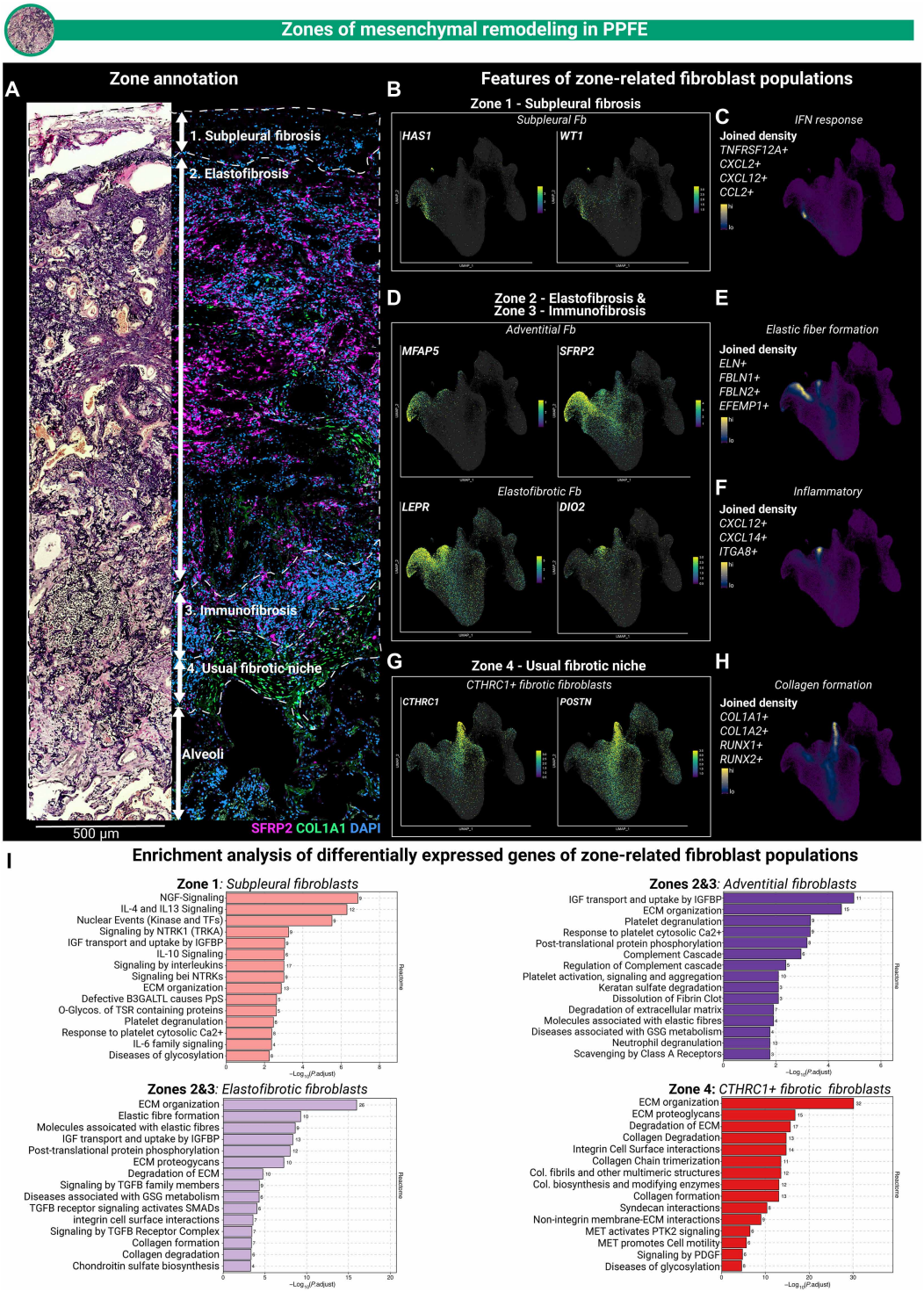

Fig. 4. Mesenchymal archetypes in the PPFE lung. (**A**) Correlative EvG- and RNA ISH–based stains of different pathogenic fibroblast (Fb) archetypes in PPFE. Serial sections illustrate spatial zonation of remodeling in PPFE. (**B**) Featureplots of signature genes expressed by subpleural fibroblasts. (**C**) Nebulosa plot of interferon response genes expressed by subpleural fibroblasts. (**D**) Featureplots of selected genes expressed in either adventitial or elastofibrotic fibroblasts. (**E**) Nebulosa plots of genes related to elastic fiber formation expressed by adventitial and elastofibrotic fibroblasts. (**F**) Nebulosa plot of inflammatory gene signature expressed by adventitial and elastofibrotic fibroblasts (**G**) Featureplots of selected genes expressed in *CTHRC1*+ fibrotic fibroblasts. (**H**) Nebulosa plots of genes related to collagen formation expressed by *CTHRC1*+ fibrotic fibroblasts. (**I**) Reactome pathway-based enrichment analysis of significantly differentially expressed genes of distinct zone-related fibroblast populations. The number behind the bar indicates the number of enriched genes per Reactome term.

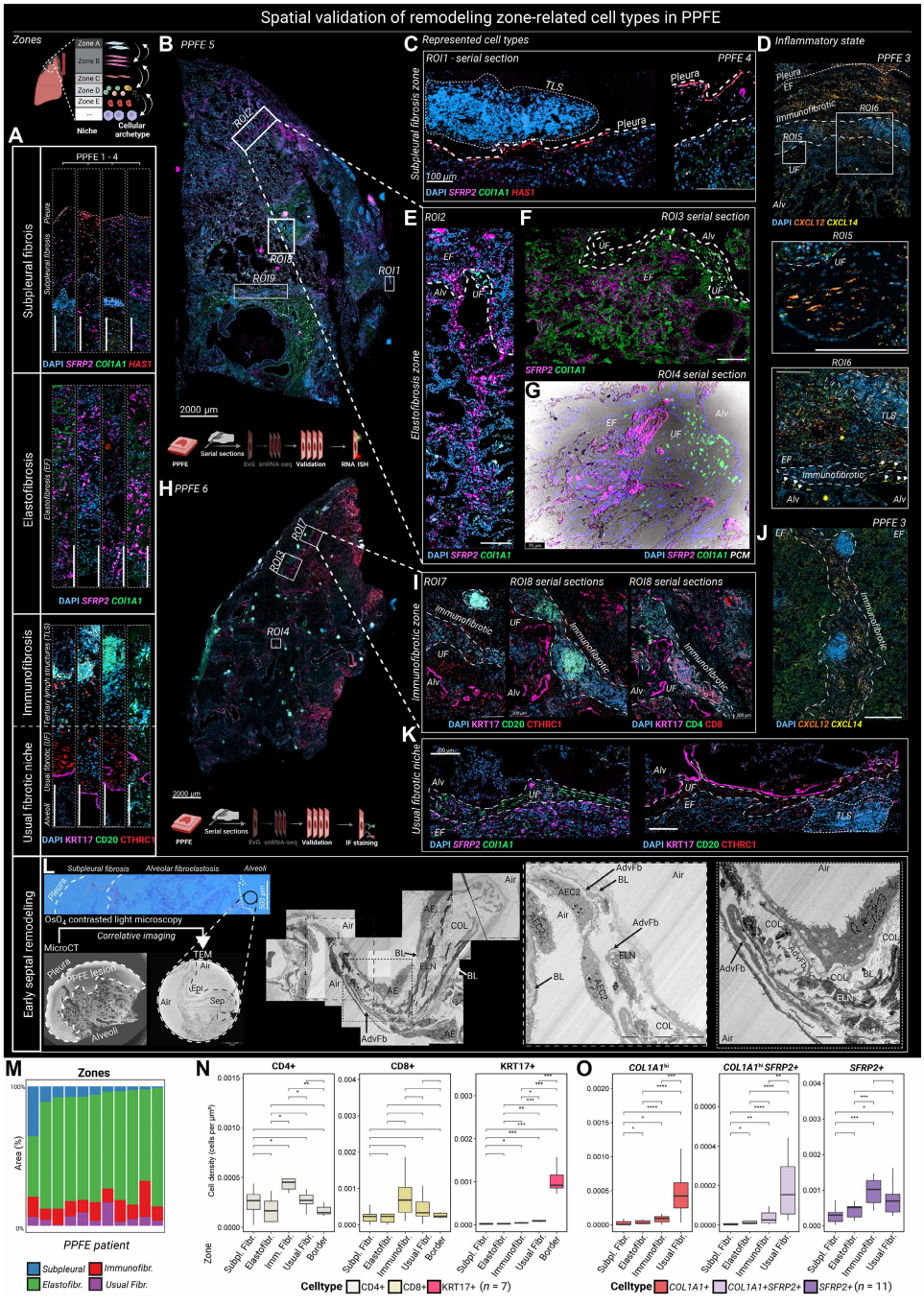

Fig. 5. Zonation in the PPFE lung. (**A**) Major zones of remodeling in PPFE indicated by IF and ISH. (**B**) Representative ISH of the upper lobe PPFE lesion at low magnification. (**C**) Representative high-magnification images of ISH staining of the subpleural fibrosis zone. Depicted TLSs emerged in the subpleural fibrosis zone in $n = 5/7$ specimens. (**D**) Representative spatial expression of inflammatory fibroblast-related chemokines. Boxes indicate a higher-magnification image of the usual fibrotic niche (ROI5) and the remodeling edge (ROI6). Pleura (fine) and immunofibrotic zone (coarse) and *CXCL14+ cells* (arrow) are highlighted. (**E**) Representative high-magnification image of septal remodeling within the aerated alveolar parenchyma. The remodeling edge is highlighted by a dashed line. (**F**) Representative high-magnification image of ISH-stained lesions of elastofibrosis adjacent to the usual fibrotic niche (dashed line). (**G**) Representative PCM overlay highlights elastic fibers. (**H**) Representative IF of the upper lobe PPFE lesion at low magnification. Boxes mark ROIs that are shown in higher magnification. (**I**) Representative high-magnification IF images of the TLS. (**J**) Representative ISH staining of the immunofibrotic zone. (**K**) Representative IF and ISH staining on serial sections of the usual fibrotic niche. (**L**) Micro-CT guided correlative imaging of early septal thickening beyond the fibroalveolar remodeling edge. Scale bars, 20 µm (low magnification) and 10 µm (high magnification). Fibroblast with adventitial fibroblast like morphology (Adv. Fb), alveolar epithelium (AE), basal lamina (BL), alveolar epithelial cells type 2 (AEC2), collagen (COL), and elastin (ELN) are annotated accordingly. (**M**) Area proportions of manually segmented remodeling zones ($n = 11$ PPFE-GER) (**N**) Cell densities of CD4+, CD8+, and KRT17+ cells per zone (IF: $n = 7$). (**O**) Calculated cell densities of *COL1A1+*, *SFRP2+COL1A1+*, and *SFRP2+* cells per zone (ISH: $n = 11$). Scale bars in ISH and IF stains represent 200 µm unless stated otherwise. Created in BioRender. Schupp, J. (2026) https://biorender.com/br8cgh6.

Aberrant basaloid cells line the fibroepithelial remodeling edge

Aberrant basaloid cells were identified with considerable frequency based on the expression of 28 marker genes (*10*), which were fully conserved in both PPFE and the IPF cohorts (Fig. 6, A to C; fig. S8; and tables S25 to S27). ssGSEA confirmed previously described pathogenic features of these cells by enrichment of gene ontology (GO) pathways involved in fibrotic pulmonary remodeling (Fig. 6D and table S28). IF staining for KRT17, COX2, ITGAV/B6, and CTSE confirmed their localization as a cellular monolayer lining the edge of elastofibrotic remodeling (Fig. 7, A to N), overlining *CTRHC1*+ fibrotic fibroblasts. This composition is known as fibroblast foci in IPF, we therefore coined their joint emergence despite a different histological gestalt "usual fibrotic niche." This spatial pattern was consistently observed in all investigated PPFE samples. Micro-CT guided ultrastructural imaging of the usual fibrotic niche visualized aberrant basaloid cells as cuboidal shaped cells with apical microvilli and numerous cytoplasmic intermediate filaments (Fig. 6E, arrows), as already reported in IPF (*37*). Within the elastofibrosis zone, we observed lesional remnants of alveoli and duct-like structures (Fig. 6F, asterisk) lined by transitional epithelial cells coexpressing AEC2 (SFTPC and LAMP3), AEC1 (AGER), basaloid (KRT17), and injury (CTSE) markers (Fig. 7, K and M, and fig. S9) not present in alveoli from CTRL lungs (fig. S10). These intermediate cells were frequently observed in alveoli adjacent to the fibroelastotic remodeling edge as well (Fig. 7, F and G, and fig. S9).

CellChat-based interaction weight analysis highlighted *CTHRC1*+ fibrotic fibroblasts as a general signaling hub with the highest connectivity to aberrant basaloid cells (Fig. 6, F and G). Major involved pathways in this unsupervised intercellular cross-talk analysis were related to secretion of collagen, laminin, thrombospondin, and fibronectin (Fig. 6, H and I). Aberrant basaloid cells express various stimulatory ligands such as *TGFB2* and *PDGFC*, with predicted activation of *CTHRC1*+ fibrotic fibroblasts in their surrounding niche via corresponding receptors (*TGFBR2*, *PDGFRB*, *PDGFRA*, and *ACVR1*; Fig. 6J).

Multimodal profiling of lesional vascular conglomerates in PPFE

Distribution of intraendothelial cell frequencies was shifted in the PPFE group toward two ectopic cell populations (Fig. 8, A to C): First, lymphatic ECs (*PDPN*, *CCL21*, and *RELN*; fig. S11, A to E, and tables S29 to S31) were increased in PPFE (adj.$P\text{val}_{\text{vs.IPF}} < 0.001$) but not in IPF (Fig. 8, B and C). IF staining of PDPN revealed an expansion of lymphatic vasculature in AFE lesions (Fig. 8, D and E). Overlay with PCM images located lymphatic ECs in the same niche as elastic fiber depositing adventitial fibroblasts (Fig. 8D). Second, we observed a relative increase in ectopic systemic-venous ECs (*COL15A1* and *PLVAP*; Fig. 8, B and C). This endothelial phenotype has recently been described in IPF lungs (*10*, *38*), nonspecific interstitial pneumonia (NSIP) (*39*), and RAS (*40*). Colocalization of PPFE-associated endothelial and mesenchymal populations (fig. S11F) prompted us to assess the underlying intercellular signaling circuits (fig. S11, G and H). Lymphatic ECs had the highest scaled ligand activity for the *BMP2-ACVR1* and *PDGFC-PDGFRA* axis for signaling toward PPFE-associated fibroblasts (fig. S11H), whereas systemic-venous ECs signaled via *JAM2-JAM3*, *JAM2-ITGB1*, and *JAM2-ITGAV* (fig. S11H). Downstream target genes in PPFE-associated fibroblasts were enriched in proteoglycan metabolism, angiogenesis, and ECM remodeling pathways (fig. S11I and table S32).

To obtain a better understanding of the three-dimensional (3D) context of the vasculature in PPFE lesions, we performed HiP-CT of the intralesional vasculature (Fig. 8F). 3D reconstruction indicated that the pronounced vascular conglomerate located at the border of the Elastofibrotic and subpleural fibrosis zone communicates with interlobar veins (Fig. 8F and movie S1), suggesting intervascular anastomosis between systemic-venous and pulmonary-venous vasculature. Micro-CT imaging of fixed lung tissue contrasted with osmium tetroxide and phosphotungstic acid confirmed numerous small vessels infiltrating the remodeled PPFE tissue originating from the alveolar parenchyma via the remodeling edge (fig. S12, A and B, white arrows). Simultaneously, we noted a subpleural vascular offspring of narrow caliber vessels with centripetal rejuvenation (fig. S12, A and B, black arrows).

DISCUSSION

With this study, we provide a binational single-nucleus RNA sequencing (snRNA-seq) atlas of the cellular and structural landscape in PPFE. On the cellular level, we observed unexpected activation states and diversity of mesenchymal cells in PPFE lesions, characterized by expression profiles reflecting a division of labor in driving elastofibrotic remodeling. We observed a pronounced expansion of lymphocytes in a disease that, to date, has been considered purely elastofibrotic. We identified *CTHRC1*+ fibrotic fibroblasts and aberrant basaloid cells in PPFE, which had previously been discovered as fibroblast foci–forming cells in IPF (*23*, *25*, *35*). On the histological level, we describe zonation of PPFE lesions, comprising the abovementioned PPFE-associated cell types. Comparison with IPF revealed common principles of lung fibrosis, especially the emergence of the usual fibrotic niche in two clinically divergent progressive fibrotic ILDs. It also highlights differences, in particular PPFE-enriched inflammatory phenotypes of all major fibroblast populations, intriguing TLS formation in close proximity to the fibrotic remodeling edge, as well as intercellular circuits that maintain the zonation of PPFE lesions.

Inflammatory fibroblast activation states have been consistently reported in murine bleomycin-induced lung fibrosis, but its role in human disease has been unclear until now (*25*–*27*). In PPFE, we show that multiple nonalveolar fibroblasts acquire such inflammatory states. Collectively, these fibroblast subtypes normally reside in the loose connective tissue space of the pleura, adventitia, and the interlobular septum. Of special interest, *CXCL12*- and *CXCL14*-expressing *LEPR+ITGA8+SFRP2+DIO2+* elastofibrotic fibroblasts (*28*) are expanded in the PPFE lung, matching the reported signature of inflammatory fibroblasts in the bleomycin model. Unexpectedly, this phenotypic subset was barely detectable in IPF, in line with recent spatial transcriptomic analyses in IPF (*23*, *35*, *36*). These inflammatory elastofibrotic fibroblasts exhibit substantial marker overlap with *CTHRC1*+ fibrotic fibroblasts, as reported for mice (*25*–*28*). In murine bleomycin-induced lung fibrosis, *Cxcl12*$^{+}$ inflammatory fibroblasts originate from alveolar fibroblasts and progressively differentiate into *Cthrc1*$^{+}$ fibrotic fibroblasts (*27*). This contrasts with PPFE, where the cellular counterparts appear to rather originate from pulmonary loose connective tissue fibroblasts. Both *CXCL12*-expressing inflammatory adventitial and elastofibrotic fibroblasts are readily found in PPFE, but not in IPF, and are spatially associated with histopathological features such as septal elastosis and elastic fiber deposition. Together, our molecular profiling of the PPFE mesenchyme emphasizes

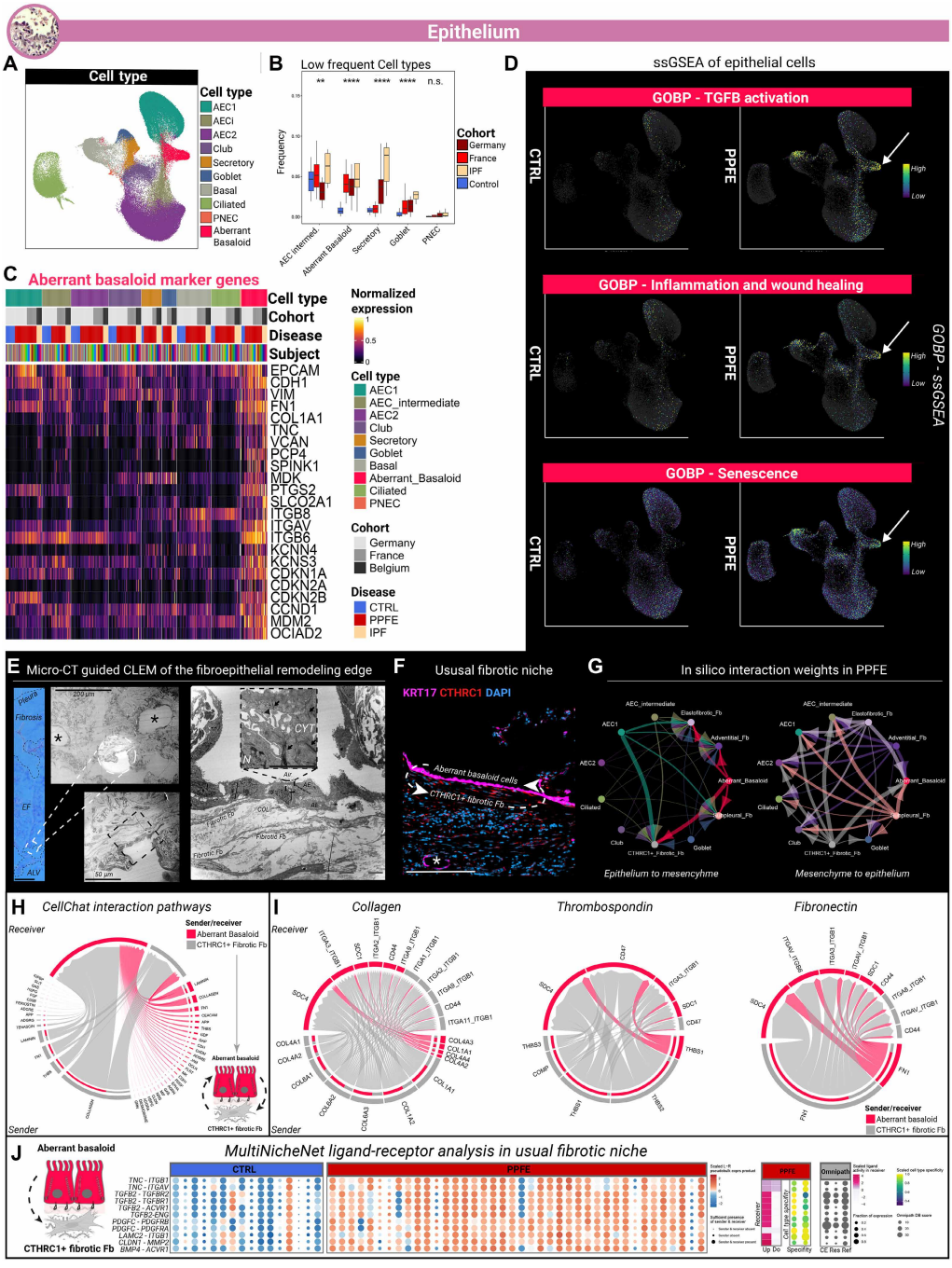

Fig. 6. Subanalysis of the epithelial cell lineage. (**A**) UMAP of epithelial cell types. (**B**) Frequencies of epithelial cell types by cohort. Statistical comparisons were performed using the Kruskal-Wallis test. Detailed results are provided in table S27. (**C**) Unity-scaled average expression of aberrant basaloid markers per subject. Subjects were grouped after cohort and disease. Each subject was assigned to a unique color. (**D**) Featureplots of cell-based ssGSEA enrichment values of distinct gene ontology biological pathways (GOBP) of fibrotic remodeling. Arrows indicate clusters of aberrant basaloid cells. (**E**) Micro-CT guided correlative imaging of early septal thickening beyond the fibroalveolar remodeling edge. Low-resolution image of osmium tetroxide–contrasted 50-μm-thick sections (left; scale bar is 500 μm). Scale bars, 50 μm (low magnification), 20 μm (medium magnification), and 10 μm (high magnification). Nuclei (N), cytoplasm (CYT), and intermediate filaments (arrows) are annotated on high-magnification images. (**F**) IF stains of the usual fibrotic niche and its overlining epithelium. (**G**) Intercellular ligand-receptor interaction weight analysis (CellChatv2) among major epithelial and mesenchymal cell types split by assigned sender lineage. Edge thickness resembles interaction weight. CTHRC1+ fibrotic fibroblasts were colored in gray for improved visual clarity. (**H**) Intercellular pathway-based interaction analysis between CTHRC1+ fibrotic fibroblasts and aberrant basaloid cells. Chord thickness corresponds to the number of predicted significant interactions between the sender and the receiver. (**I**) Chord diagram of predicted intercellular ligand-receptor pairs between aberrant basaloid cells and CTHRC1+ fibrotic fibroblasts related to top 3 pathways predicted in (H). (**J**) MultiNicheNetR differential ligand-receptor analysis between PPFE and CTRL focused on aberrant basaloid–to–CTHRC1+ fibrotic fibroblast signaling. Omnipath-related metadata like curation effort (CE), the number of available resources (Res), and the number of references found (Ref) are also provided. Created in BioRender. Schupp, J. (2026) https://biorender.com/br8cgh6.

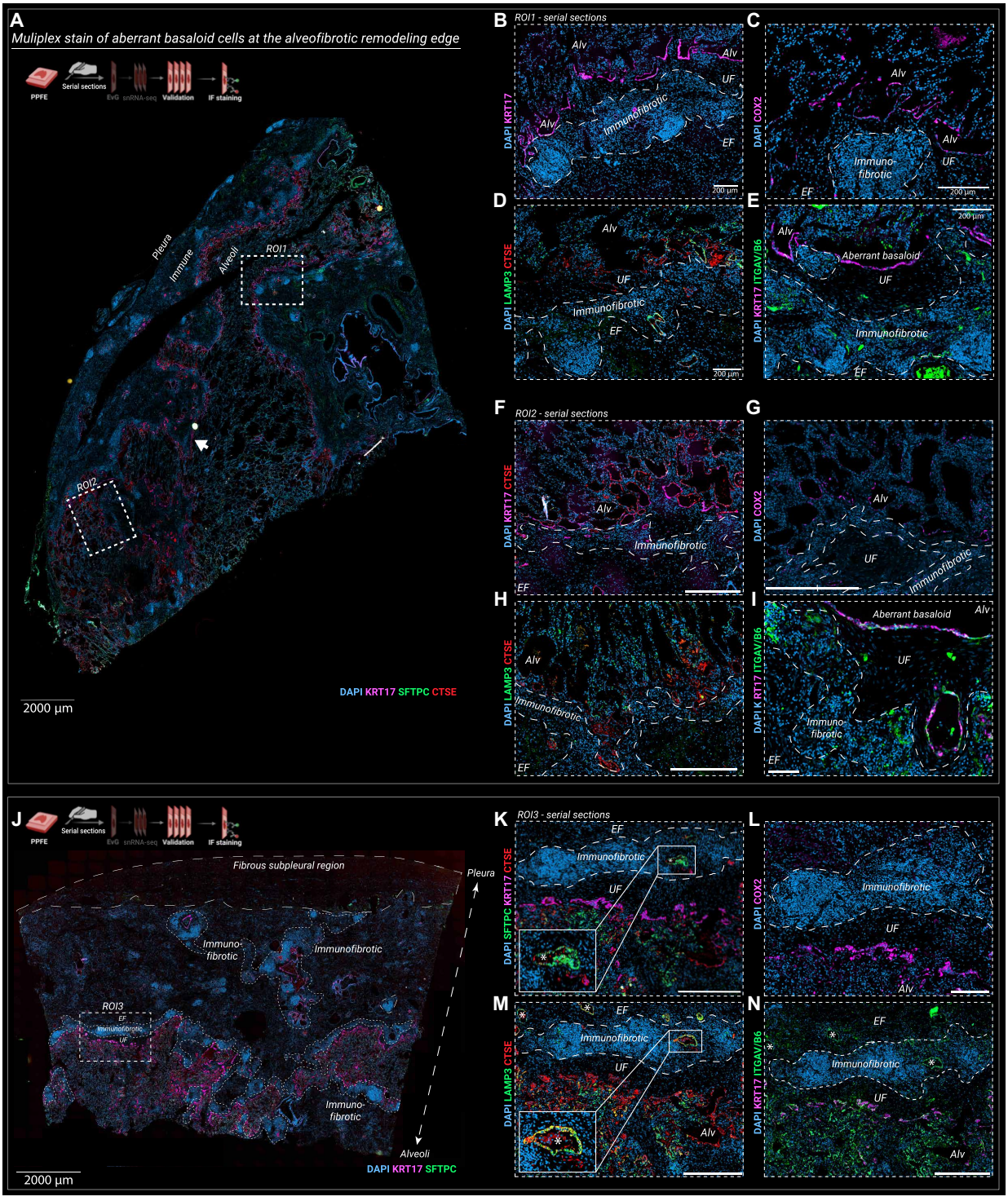

Fig. 7. IF staining of aberrant basaloid cells in the PPFE lung. (**A**) Representative low-magnification image of whole-slide IF-stained PPFE specimens. Dashed boxes indicate ROIs. The arrow indicates the fibroepithelial remodeling edge. (**B** to **I**) Representative high-magnification images of aberrant basaloid marker genes on serially sectioned tissue specimens. The immunofibrotic zone is highlighted by a dashed line. (**J**) Representative low-magnification image of whole-slide IF-stained PPFE specimens with pronounced subpleural fibrosis (coarse dashed line). Dashed boxes indicate ROIs. The immunofibrotic zone is highlighted as well (fine dashed line). (**K** to **N**) Representative high-magnification images of aberrant basaloid marker genes on serially sectioned tissue specimens. The immunofibrotic zone is highlighted by a dashed line. An intralesional remnant of alveoli (*) formed by epithelial cells being copositive for LAMP3 and CTSE is shown with high magnification. The elastofibrosis zone (EF), usual fibrotic niche (UF), and alveoli (Alv) are annotated throughout IF stains. IF images of control specimens are provided in fig. S9. Scale bars are 200 µm unless stated otherwise. Created in BioRender. Schupp, J. (2026) https://biorender.com/br8cgh6.

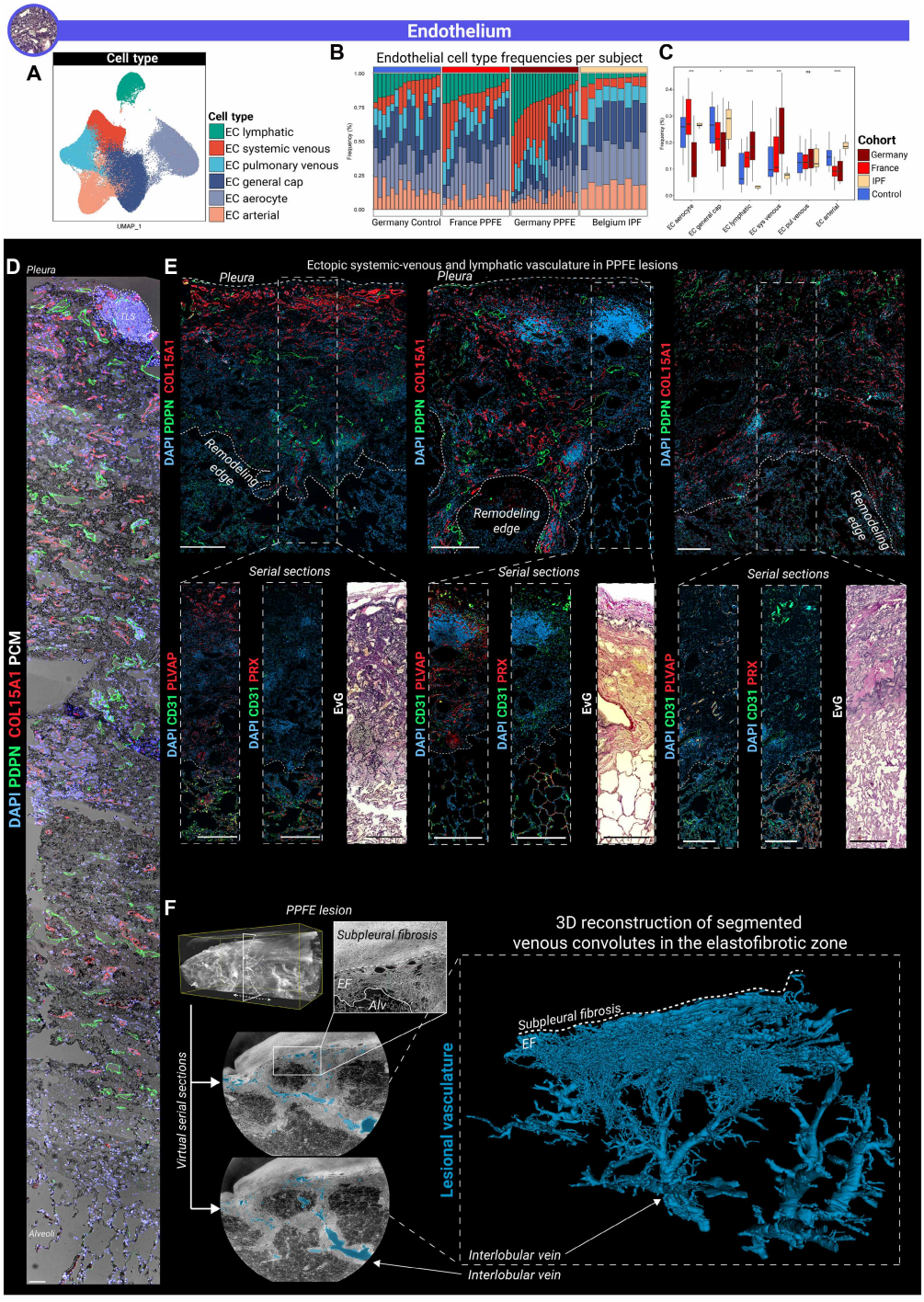

Fig. 8. Ectopic ECs in PPFE. (**A**) UMAP embedding by EC type. (**B**) Stacked bar plots of cell type frequencies per subject colored by cell type and split by cohort. Subjects were ordered after frequencies of lymphatic ECs. (**C**) Box plots display the relative distribution of each EC type relative to the total endothelial lineage compartment, stratified by disease-related cohort. Whiskers indicate 1.5 times the IQR. Statistical comparisons between PPFE-GER, PPFE-FR, CTRL, and IPF were performed using the Kruskal-Wallis test. Post hoc tests were performed under the use of the Wilcoxon rank sum test, with Bonferroni correction for multiple comparisons across cohorts and cell types. Detailed results are provided in table S30. (**D**) Representative overlay of PCM and IF staining for PDPN and COL15A1 across all remodeling zones from pleura to alveolar spaces. A TLS is encircled by a dashed line adjacent to the pleura. Scale bar, 200 μm. (**E**) Representative IF staining of vascular markers in serially sectioned subpleural PPFE lesions for lymphatic EC (PDPN), systemic-venous EC (COL15A1 and PLVAP), and aerocytes (PRX). Scale bars represent 200 μm unless stated otherwise. Pleura and remodeling edge are annotated by dashed lines. High-magnification images were complemented with serially sectioned EvG stains. The left EvG subimage was intentionally reused from Fig. 4A. (**F**) Zoomed HiP-CT image of PPFE lesions located in the upper lobe. Pulmonary vein segmentation was performed using an adopted nnU-Net framework. The resulting segmentation of the ectopic vasculature (blue) shows the main vessel structures from the highlighted region, illustrating an interconnection of interlobular veins and venous convolutes at the border of subpleural and elastofibrotic remodeling.

the relevance of inflammatory fibroblast states for elastofibrotic remodeling in human disease.

The role of inflammation in lung fibrosis has remained controversial over decades. On the one hand, various autoimmune diseases can lead to fibrotic remodeling of the lung, with inflammatory changes usually preceding the development of definitive fibrosis (*41*–*43*). On the other hand, fibrosis can cause inflammation as fibrotic remodeling itself induces autoantigen shedding with consecutive autoantibody formation (*44*). In addition, patients with fibrotic ILD exhibit a dysregulated immune compartment with expansion of regulatory T cells, GZM^{high} CD4+, and CD8+ effector T cells (*14, 45*). However, untargeted immunosuppression increases mortality in IPF, especially in patients with short telomers (*46, 47*), which has also been observed in telomeropathy-associated PPFE (*47*–*49*). Therefore, anti-inflammatory treatment regimen are rarely tested in fibrotic lung diseases. Our work highlights accumulating immune cells forming TLSs and accompanying inflammatory fibroblasts as integral components of the cellular landscape of PPFE, providing a molecular rationale for niche-specific therapeutic strategies. This may apply beyond PPFE as *SFRP2*+ fibroblasts have been described as myofibroblast precursors in systemic sclerosis skin lesions (*50*), and *CXCL12*+ fibroblasts shape the TLS-related stromal niche in various cancers (*32*) as well as driving fibrotic bone marrow remodeling in primary myelofibrosis (*51*). In the lung, inflammatory fibroblasts appear to serve as orchestrators of immune cell recruitment and TLS formation culminating in downstream formation of the usual fibrotic niche. Hence, our work raises the question whether targeting inflammatory fibroblasts or TLS formation by interference with the central *CXCL12-CXCR4* axis could alleviate immunofibrotic remodeling in PPFE.

The divergent radiological and histopathological features of PPFE and IPF suggest different disease processes. It was somewhat unexpected then that *CTHRC1*+ fibrotic fibroblasts and aberrant basaloid cells emerged in the PPFE lung as well. As both pathological cell types replicate their intercellular framework in both PPFE and IPF, we emphasize their spatial coemergence as "usual fibrotic niche." Aberrant basaloid cells are the key players in fibrotic remodeling due to their unique characteristics of transforming growth factor–β (TGFβ) activation, senescence, and injury memory (*10*), whereas *CTHRC1*+ fibrotic fibroblasts secrete immature collagen (*33*, *34*). Since their discovery a few years ago, an increasing number of single-cell (*10*, *13*, *40*, *42*) and spatial transcriptomic (*23*, *35*, *36*) studies have reported aberrant basaloid cells in IPF and other fibrotic lung diseases. In the IPF lung, *CTHRC1*+ fibrotic fibroblasts aggregate to fibroblast foci, which are covered by aberrant basaloid cells (*10*, *13*, *23*, *35*, *36*). In contrast to IPF, the site of active remodeling of PPFE is not a patchy chaotic mosaic but a continuous layer at the alveolofibrotic remodeling edge (Fig. 9C). PPFE as a disease highlights therefore that the usual fibrotic niche is more common than previously anticipated and not limited to the gestalt of fibroblastic foci.

The loss of *CD31*+*PRX*+ capillaries and the emergence of ectopic *COL15A1*+ *PLVAP*+ vessels (*38*) shown in the herein investigated PPFE cohorts have been consistently reported in IPF (*10*), NSIP (*39*), and RAS (*40*). The extent and communication of ectopic *COL15A1*+ *PLVAP*+ vascular convolutes in the elastofibrosis zone with interlobular pulmonary veins in the 3D HiP-CT segmentation in the PPFE lung are somewhat unexpected. In contrast to IPF, we observed an expansion of lymphatic ECs, localized to the subpleural and interlobular lymphatic vasculature. *CCL21*+*PDPN*+ lymphatic ECs may enhance recruitment of *SELL*-expressing naïve T cells to sites of ongoing elastofibrotic remodeling, further shaping the micromilieu of the immunofibrotic zone. Together, our PPFE study supports that the observed alveolar vascular remodeling is a general phenomenon of fibrotic ILD and elaborates on the unique contribution of the lymphatics to elastofibrotic remodeling.

To contextualize these findings, we offer the following hypothetical working model of PPFE development: We observed a strong inflammatory activation in fibroblasts related to the loose connective tissue compartment of the pleura and the peribronchovascular bundle (Fig. 9A), suggesting an initial hit there. Inflammation-activated local adventitial and subpleural fibroblasts secrete cytokines such as CCL2, CXCL2, CXCL12, and CXCL14, recruiting *CXCR4*+ lymphoid and *CSFR*+ monocytic cell populations. Incoming CD20+ B cell and CD4+ and CD8+ T cell populations assemble as TLSs at the site of injury orchestrated by local CXCL12/13 gradients (Fig. 9B). TGFB1 in the (peri)-TLS niche further drives particularly inflammatory adventitial fibroblasts to transition first into *CXCL14*-expressing *LEPR*+*ITGA8*+*DIO2*+ elastofibrotic fibroblasts, which might promote interstitial elastotic and fibrotic remodeling (Fig. 9C). These cells may then transition into *CTHRC1*+ fibrotic fibroblasts that fill former alveoli with collagens and proteoglycans. Matrix stiffening and altered basal membrane composition may then trigger epithelial dedifferentiation into aberrant basaloid cells (Fig. 9D), which—together with *CTHRC1*+ fibroblasts—form the usual fibrotic niche and sustain mesenchymal activation through TGFB2 and integrin activation. Recruited immune cells then amplify inflammatory fibroblasts to acquire a metabolic active state characterized by excessive interstitial deposition of elastic fibers along the alveolar septa. Together, this continuously would lead to propagation of the elastofibrotic remodeling deeper into the yet intact alveolar parenchyma (Fig. 9E).

Our study is not without limitations. First, the investigated cohorts are restricted to two countries in Western Europe, which may limit the external validity of our findings. Second, the CTRL subjects were not fully matched to patients with PPFE with respect to age and smoking status. In particular, the CTRL cohort was, on average, younger and included a higher proportion of current or former smokers. Consequently, disease-associated changes may, at least in part, be influenced by these demographic differences between cohorts. However, age-related effects on alveolar cell composition reported in a recent scRNA-seq study include a relative loss of *SFTPC*-expressing AEC2 cells and a concomitant increase in ciliated cells (*52*). In this context, the pronounced reduction in AEC2 frequencies observed in the comparatively younger PPFE cohorts in our study makes it unlikely that this observation, among others, is solely driven by sociodemographic differences between cohorts. Third, we integrated snRNA-seq data generated with different chemistries (10X Flex and 3′ Prime), which potentially has led to a loss of biological information due to batch correction.

In summary, this study represents an unprecedented cellular survey of PPFE, in which ectopic and aberrant cell populations spatially organize in a unique zonation pattern. We reveal PPFE-enriched inflammatory fibroblast activation states underlying the immunofibrotic remodeling that promote elastosis and highlight aberrant basaloid cells and *CTHRC1*+ fibrotic fibroblasts as core constituents of the usual fibrotic niche, driving collagenous fibrotic remodeling. The PPFE atlas is accompanied by an easily accessible webtool and provides a molecular rationale for PPFE-targeting and ILD-overarching niche-specific therapeutic strategies.

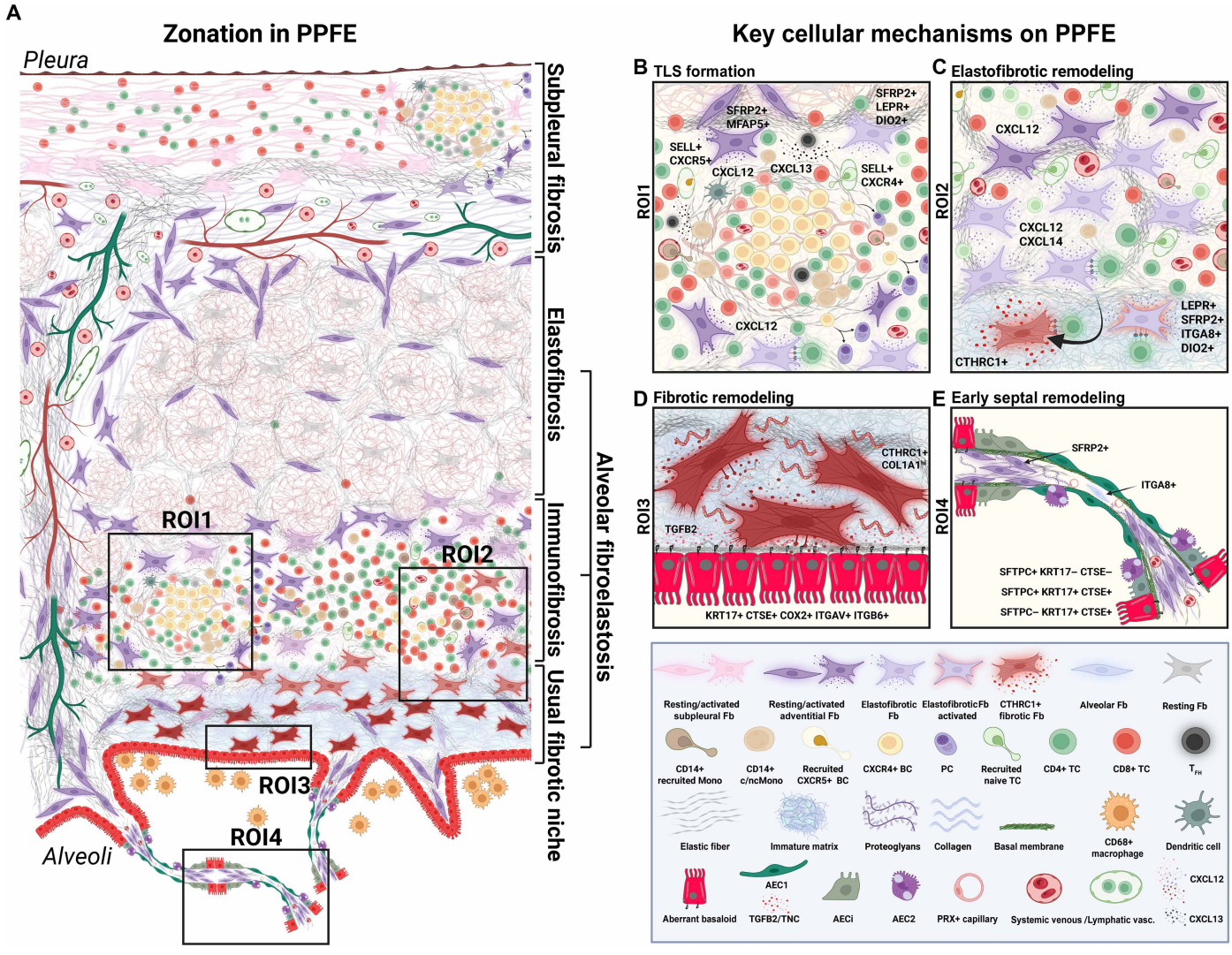

Fig. 9. Niches of remodeling in PPFE. (**A**) Schematic overview of distinct remodeling-related niches in PPFE exemplified in four zoomed-in ROIs. (**B**) Inflammatory fibroblasts (Fb) mediate formation of TLSs orchestrated by secretion of the CXCL12, a chemoattractant for naïve T cells (TC). (**C**) Activated adventitial fibroblast start expressing inflammatory and metabolic markers acquiring an elastofibrotic phenotype. Coexpression of *LEPR* and *ITGA8* identify these as a transitional inflammatory state differentiating in *CTHRC1*+ fibrotic fibroblasts mediated by local recruited immune cells. (**D**) *CHTRC1*+ fibrotic fibroblasts drive alveolar filling with the ECM and collagens coinciding with alveolar epithelial cell (AEC) dedifferentiation into aberrant basaloid cells, which further perpetuate local fibrogenesis via TGFB2 secretion. (**E**) Early septal thickening within yet less affected alveolar parenchyma on the other side of the elastofibrotic remodeling edge may be driven by activated elastotic adventitial fibroblasts originating from the loose connective tissue space of the pleura, interlobular septa, or bronchovascular bundle that expand into the alveolar interstitium. c/ncMono, classical and nonclassical monocytes; BC, B cells; PC, plasma cells; T_{FH}, T follicular helper cells as T_{FH}; vasc., vasculature. Created in BioRender. Schupp, J. (2026) https://biorender.com/br8cgh6.

MATERIALS AND METHODS

Experimental design

The aim of this binational, cross-sectional snRNA-seq study was to characterize the single-cell landscape of PPFE and to dissect cellular circuits linked to the specific histopathological pattern of AFE. Therefore, we enrolled 40 patients with PPFE, 23 from Germany (PPFE-GER) and 17 from France (PPFE-FR), who had undergone lung transplantation. Lung tissue from downsizing lungs and peripheral tumor resections ($n = 7$) together with nine controls published previously by our group (GSE284081) served as control (CTRL; total $n = 16$). Our IPF snRNA-seq data [$n = 9$; GSE286182 (*19*)] served as disease comparator. Diagnosis of PPFE was established in concordance with current guidelines on multidisciplinary team discussions (*1*). CT pattern fulfilling the criteria of "definite" or "consistent with" PPFE were considered eligible for the study. Samples from patients that had undergone retransplantation due to RAS were excluded. Tissue samples from included patients were evaluated by histological stains (EvG or orcein staining; $n = 40$) and micro-CT imaging ($n = 10$). Samples were selected for further analysis in this study if AFE was present. One formalin-fixed paraffin-embedded (FFPE) block per patient was selected for further processing. Written informed consent was obtained from all subjects. The study was approved by the local ethics committee of the Hannover Medical School of Hannover, Germany (ethic vote #11032_BO_K_2023), APHP, Bichat Hospital (Comite de Protection des Personnes Ile de

France 1, no. 0811760) and Marie Lannelongue Hospital (Ministère de l'Enseignement Supérieur de la Recherche et de l'Innovation, AC-2020-4284).

Validation experiments were performed using multiplex IF and ISH on serially sectioned FFPE specimens. For linking the single-cell resolved transcriptome with cellular ultrastructure, we performed correlative ultrastructural analysis (CUA). Analysis of vascular PPFE hallmark lesions was complemented with micro-CT and HiP-CT for providing 3D context. Blinding or randomization was not performed in this study.

Single-nucleus RNA sequencing

For snRNA-seq, nuclei were isolated from three 50-µm-thick FFPE sections of each selected block. Following 4′,6-diamidino-2-phenylindole (DAPI) sorting, nuclei were further processed in accordance with the 10X fixed RNA profiling kit (User Guide, CG000527, Rev B, Chromium Fixed RNA Profiling Reagent Kits for Multiplexed Samples), specifying a target recovery of 128,000 nuclei per 16 samples, which were then loaded on the 10X Chromium Chip (Chromium Next GEM Chip Q). Following quality control of the resultant libraries, sequencing was performed on an Illumina NovaSeq platform (28 base pairs for Read1, 90 base pairs for Read2, and 10 base pairs for Index5 and Index7). Resultant sequencing data were subjected to the Cell Ranger pipeline (v7.1.0), and reads were mapped to the reference genome (GENCODE v32/Ensembl 98, "GRCh38-2020-A"). The count matrices were further analyzed using the Seurat pipeline (R package Seurat v4.3.0.1) in R (v4.2.1, The R Foundation), following the developer's recommendations for scRNA-seq data processing and dataset integration.

In brief, low-quality filtering was conducted in an iterative adaptive manner per sample, following normalization, scaling, dimensionality reduction, and plotting of lineage marker genes to control for information loss while filtering. Minimum read counts were set to 100, whereas minimum feature counts were set 100 as well. Nuclei exceeding minimum >15% mitochondrial reads were filtered out before downstream analysis. Following normalization, a scale factor of 10,000 unique molecular identifiers (UMIs) per cell downstream integration was performed on sample level for the 23 German PPFE, 17 French PPFE, and 16 German CTRL datasets. For integration, we used Seurat's reciprocal principal components analysis (RPCA) integration algorithm. Prior, Seurat's FindVariableGenes() (default settings with nFeatures = 2000) function was used for feature reduction. Following scaling, clustering was performed with the Louvain algorithm and cell type annotation was carried out on the basis of identification of canonical marker gene expression collapsed to subject level that were matched to cell type annotations of published resources (*13, 19, 27, 28, 38, 53, 54*).

A snRNA-seq dataset from nine patients with IPF sampled at three distinct lung regions each (GSE286182) (*19*) was integrated with the PPFE and CTRL data to serve as disease control. Being mapped to a distinct reference genome (GENCODE_release37_GRCh38.p13), gene names were translated into their corresponding gene names from release version 32 under usage of the biomaRt suite and the respective gene annotation databases from ensembl (https://ensembl.org/index.html?redirect=no; last accessed 11 November 2024). Only features available in the 10X Flex assay were used for further downstream data analysis. Following further data preprocessing as indicated above, IPF snRNA-seq data were integrated sample-wise with PPFE and CTRL samples running Seurat's RPCA-based reference-based integration considering samples derived from the main cohort as a reference to avoid major batch effect due to distinct sets of features and chemistry. Samples per patient were pooled before statistical cell frequency analysis. Following integration, downstream dimensionality reduction, graphical embedding, clustering, and cell type annotation were performed as described above.

Details on quality control, cell type annotation, and downstream in silico analyses are provided in the Supplementary Materials (table S3).

Immunohistochemistry

IHC was conducted to evaluate the functionality and accuracy of primary antibodies (table S1). A standard deparaffinization and rehydration procedure for FFPE tissue was carried out (2x 5 min xylene, 2x 3 min 100% ethanol, 1x 3 min 95% ethanol, 1x 1 min 70% ethanol, 1x 1 min 50% ethanol, and 1x 5 min distilled water), followed by heat-induced antigen retrieval. Tissue slides were heated for 20 min at 98°C in a 1× Tris-based Antigen Unmasking Solution (Vector Laboratories, USA), which was diluted 1:100 with distilled water. After allowing the specimens to cool for 20 min, they were washed in 1x phosphate-buffered saline (PBS) for 5 min. Following placement of a hydrophobic barrier (Roth-Liquid Barrier Marker), specimens were incubated for 10 min in BLOXALL Endogenous Peroxidase and Alkaline Phosphatase Blocking Solution (Vector Laboratories, USA). Tissue slides were then washed for 5 min in 1x PBS and blocked for 20 min using a 2.5% Normal Horse Serum Blocking Solution (Vector Laboratories, USA). Each specimen was incubated for 30 min with a primary antibody at room temperature. Following an additional washing step, each specimen was incubated for 30 min with a corresponding secondary antibody (anti-mouse, anti-rabbit, or anti-goat ImmPRESS reagent, conjugated with horseradish peroxidase, Vector Laboratories, USA) at room temperature. The slides were washed again for 5 min in 1x PBS and then incubated for 6 to 10 min in the ImmPACT DAB Substrate Kit, Peroxidase (HRP) (Vector Laboratories, USA). The incubation time varied due to individual reaction times. After one final wash for 5 min in 1x PBS, specimens were counterstained in Hematoxylin Solution Gill no. 1 (Sigma-Aldrich, USA) for 3 min and then washed for 15 min in tap water. Subsequently, a standard dehydration in ethanol/xylene was performed (1x 15 s 50% ethanol, 1x 15 s 70% ethanol, 1x 1 min 95% ethanol, 2x 1 min 100% ethanol, and 2x 3 min xylene). Tissue slides were mounted with VectaMount permanent mounting solution (Vector Laboratories, USA), and coverslips were placed on top. Stained slides were digitized and analyzed using a ZEISS Axioscan 7 and the ZEN 3.5 (blue edition) software.

IF staining

A standard deparaffinization and rehydration of FFPE tissue was carried out (2x 5 min xylene, 2x 3 min 100% ethanol, 1x 3 min 95% ethanol, 1x 1 min 70% ethanol, 1x 1 min 50% ethanol, and 1x 5 min distilled water), followed by heat-induced antigen retrieval. For this, FFPE tissue slides were heated for 20 min at 98°C in 1× Tris-based Antigen Unmasking Solution (Vector Laboratories, USA), which was diluted 1:100 with distilled water. Afterward, specimens were cooled for 20 min in 1x PBS at room temperature. A stock solution of 0.9995x PBS and 0.05% Tween 20 was prepared to create 2.5% normal serum (donkey/goat/horse) corresponding to the species of the secondary antibodies. All primary and secondary antibodies were diluted in the appropriate 2.5% normal serum and stored at room temperature under aluminum foil until required. Once the slides cooled, they were circled with a Roth-Liquid Barrier Marker and placed in a wet chamber used for storing slides during all subsequent incubation steps. Specimens were incubated for 20 min with 2.5% normal serum. Each

specimen was then incubated for 60 min with the prepared solution of 2.5% normal serum and primary antibody/antibodies at room temperature. Slides were washed for 2x 3 min in PBS containing 0.05% Tween 20. Specimens were subsequently incubated for 60 min with the prepared solution of 2.5% normal serum and secondary antibody/antibodies under aluminum foil at room temperature. The slides were washed in staining vessels covered with aluminum foil for 2x 3 min in PBS containing 0.05% Tween 20. Specimens were incubated for 60 min with the prepared solution of 2.5% normal serum and fluorochrome-conjugated antibody/antibodies under aluminum foil at room temperature. Slides were washed in staining vessels covered with aluminum foil for 2x 3 min in PBS containing 0.05% Tween 20. The Vector TrueView Autofluorescence Quenching Kit (Biozol, VEC-SP-8400-15) was used according to the manufacturer's instructions before washing slides in staining vessels covered with aluminum foil for 5 min in PBS containing 0.05% Tween 20. Last, slides were mounted using the VECTASHIELD Vibrance with DAPI Antifade Mounting Medium (Vector Laboratories/Biozol, VEC-H-1800), and coverslips were placed on top. Stained slides were digitized and analyzed using a ZEISS Axioscan 7 and the ZEN 3.5 (blue edition) software. The slides were stored in the dark at 4°C.

Primary and secondary antibodies

All primary antibodies were prevalidated through repeated testing on appropriate tissue types using both IHC and IF to ensure specific and robust staining. The primary antibodies used for IF and EvG-IHC staining of PPFE and CTRL samples are listed in table S1. Secondary antibodies for IF were similarly preevaluated in combination with well-characterized primary antibodies to confirm consistent performance.

RNA ISH

RNA ISH was conducted in adherence to the "RNAscope Multiplex Fluorescent Reagent Kit v2 User Manual" (UM 323100/Rev B; effective date: 10 November 2022) from ACDBio on FFPE lung explant tissue. Two to three target probes were multiplexed during the assay in combination with conventional DAPI staining provided by the kit. The probes used are detailed in table S2. Post-staining, slides were preserved at 4°C in a dark environment until scanning. Digitalization and analysis of the stained slides were carried out using a ZEISS Axioscan 7 combined with ZEN 3.5 (blue edition) software.

Orcein and EvG staining

FFPE tissue sections underwent standard deparaffinization and rehydration (1:30 min in xylene, followed by 1:30 min each in 100, 90, and 70% ethanol). Subsequently, German sections were incubated for 10 min in resorcinol-fuchsin solution according to Weigert, followed by differentiation in 100% ethanol (2 × 0:30 min). Iron hematoxylin staining (Weigert's method) was performed for 10 min, and sections were blued in tap water for 5 min. Slides were then counterstained in Van Gieson's solution (picrofuchsin) for 15 s. Meanwhile, French samples were stained with orcein according to the manufacturer's instructions. Dehydration was carried out sequentially (0:05 min in 70% ethanol, 1:30 min in 90% ethanol, 2 × 1:30 min in 100% ethanol, and 1:30 min in xylene). Stained sections were digitized using a ZEISS Axioscan 7 and analyzed with ZEN 3.5 (blue edition) software. Slides were stored at room temperature.

HiP-CT imaging

HiP-CT imaging was performed on the formalin-inflated lung lobe [$n = 1$ (*20*)] as described before (*55*). Virtual tissue cores were scanned within the intact inflated, formalin-fixed lung tissue. Raw images were processed with the neuroglancer pipeline (https://neuroglancer-docs.web.app/index.html). Pulmonary vein segmentation was performed on the zoomed HiP-CT data using an in-house adopted nnU-Net framework. This framework has been trained on HiP-CT and micro-CT images at different resolutions, enabling it to handle diverse input data types. The resulting segmentation from the framework has been manually revised and corrected by a lung radiologist with >15 years of experience. To enhance visual clarity, the 3D visualization shows the main vessel structures from the highlighted region and was created in 3D Slicer 3.8.1.

Micro-CT imaging

PPFE specimens were contrast enhanced using either tungsten phosphoric acid (48 hours) or osmium tetroxide (12 hours). In brief, the samples were first washed six times for 15 min each in cacodylate buffer. Postfixation was carried out by incubating the samples in 1% osmium tetroxide for 4 hours on a rotator. Following fixation, the samples were rinsed twice for 15 min in cacodylate buffer. This was followed by eight washes of 10 min each in distilled water. The samples were then incubated overnight in 1% uranyl acetate. On the next day, they were washed 12 times for 10 min in cacodylate buffer. Dehydration was performed in a graded acetone series, consisting of four steps of 30 min each in 70% acetone, followed by four steps of 30 min each in 90% acetone, and, last, six steps of 30 min each in 100% dry acetone. Contrasted formalin-fixed PPFE tissue specimen or native FFPE blocks were subsequently scanned with a Phoenix Nanotom M micro-CT system (Waygate Technologies). Imaging was performed at a voxel resolution of 8.46 µm using an x-ray tube voltage of 60 kV and a current of 110 µA. Micrographs were captured with an average dynamic range of >2000 gray levels to ensure optimal contrast. Raw data underwent preprocessing, including region of interest (ROI) selection and inline median filtering, before 3D volume reconstruction using VGSTUDIO 2022 (64-bit, Volume Graphics).

Correlative ultrastructure analysis

CUA was carried out as recently described (*56*). In brief, the osmium tetroxide–contrasted OCT embedded tissue specimen was sectioned on a cryostat (Leica, Wetzlar, German) in 50-µm-thick sections. Sections were subsequently fixed overnight with 1.5% paraformaldehyde and 1.5% glutaraldehyde in 0.15 M Hepes buffer (pH 7.35). Afterward, sections were postfixed in 1% uranyl acetate (Serva, Heidelberg, Germany) overnight and in 1% osmium tetroxide (EMS, Hatfield, PA) for 2 hours, followed by a washing step and dehydration in acetone and, last, embedding in Epon (Serva, Heidelberg, Germany). Ultrathin sections were imaged using a transmission electron microscope (model 364, Morgagni 268, FEI, Eindhoven, The Netherlands). Final correlation of TEM images and light microscopy images was performed manually. Single obtained electron microscopy images were manually stitched together for improved parenchymal context.

Image processing

Qualitative image analysis and processing of histological sections were carried out using ZEN (blue edition) software (ZEISS). For all IF and RNA ISH images, the "background subtraction" function was

applied using default parameters. White and black point values were manually adjusted for each channel. No additional image processing techniques were used. Multipanel figure assembly was performed using Adobe Illustrator 2024.

Cell segmentation and semiautomated cell quantification

For quantitative image analysis, IF or ISH scans were loaded into QuPath (0.5.1) (*57*). Cell segmentation was carried out on the basis of DAPI stains using the StarDist extension (*58*) following the recommended QuPath workflow referred to in the Docs (https://qupath.readthedocs.io/en/stable/). For StarDist-based cell segmentation, percentile normalization was applied using the 1st and 99th percentiles. A probability threshold of 0.5 was set for object detection. The analysis was conducted at a resolution of 0.5 µm per pixel. Detected nuclei were expanded by 5 µm to approximate whole-cell boundaries, with cell expansion constrained to 40% of the nuclear size to avoid overestimation. Shape descriptors and intensity measurements were calculated across all cellular compartments. Prediction probabilities were included as an additional measurement parameter. Segmented cell masks were subsequently used for manual defining channel-wise training data for the QuPath inbuilt artificial neural network (ANN) classifier. Approximately 30 to 50 cells per channel per slide were manually annotated as signal positive or negative (e.g., *SFRP2*+ versus *SFRP2*−) and used as a training dataset for the ANN classifier. Next, ANN was used for automated annotation of segmented cells as being positive or negative. Channel-related ANN-based classifications of cells were carefully reviewed. Following application of the trained classifier to the corresponding whole-slide scan, the assigned feature classes per cell per channel were exported as CellxFeature class matrices to .txt files. Zones of interest (i.e., subpleural fibrosis zone, elastofibrosis zone, immunofibrotic zone, and usual fibrotic niche) were manually segmented and annotated on the same slide in agreement with two board-certified pathologists with extensive experience in histopathological diagnostics of ILDs. Area size was exported to R, and cell densities per surface unit (μm^2) were calculated. For evaluation of the regional enrichment of *CXCL12*, 10 to 12 ROIs per slide ($n = 5$) adjacent to or not adjacent to TLSs were subsampled. Median channel intensities per cell were normalized and scaled to allow across slide comparison. For statistical enrichment analysis, an upper quantile cutoff of 0.75 was defined, followed by $n = 10{,}000$ permutations. Remodeled and unremodeled parenchymal surface fractions of PPFE samples were likewise manually annotated on serially sectioned EvG or orcein-stained slides matched to the used 50-µm slides used for nuclei isolation.

Web tool

The interactive dataset explorer of the integrated PPFE atlas dataset was assembled with the R package ShinyCell (*59*).

Statistical analysis

Statistical analyses of cell frequencies and spatial cell type densities were performed with the Kruskal-Wallis test. Post hoc intergroup analysis was conducted with the Wilcoxon rank sum test applying Bonferroni correction for multiple testing on the cell type and cohort level. Pearson correlation was used for assessing the relationship between the fraction of cells per lineage and the fraction of remodeled parenchyma per sample. Pearson and Spearman metrics were used to assess correlations between the TLS extent and the area of segmented remodeling zones. Statistical methods used throughout the snRNA-seq analysis pipeline are specified in the respective section of the methods. P values < 0.05 were considered statistically significant. Significance levels are indicated as follows: $^{*}P \leq 0.05$, $^{**}P \leq 0.01$, $^{***}P \leq 0.001$, and $^{****}P \leq 0.0001$. All statistical analyses were computed in R (v. 4.2.1, The R Foundation).

Supplementary Materials

The PDF file includes:

Supplementary Text
Supplementary Materials and Methods
Figs. S1 to S12
Legends for tables S1 to S32
Legend for movie S1
References

Other Supplementary Material for this manuscript includes the following:

Tables S1 to S32
Movie S1

REFERENCES

1. F. Chua, S. R. Desai, A. G. Nicholson, A. Devaraj, E. Renzoni, A. Rice, A. U. Wells, Pleuroparenchymal fibroelastosis a review of clinical, radiological, and pathological characteristics. *Ann. Am. Thorac. Soc.* **16**, 1351–1359 (2019).
2. H. Clermidy, O. Mercier, G. Brioude, P. Mordant, G. Fadel, C. Picard, E. Chatron, J. L. Pavec, A. Roux, M. Reynaud-Gaubert, J. Messika, A. Olland, X. Demant, T. Degot, P. Lavrut, J. Jougon, E. Sage, E. Fadel, P. Thomas, V. Cottin, F. Tronc, Outcomes of lung transplantation for pleuroparenchymal fibroelastosis: A French multicentric retrospective study. *J. Heart Lung Transplant.* **43**, 1727–1736 (2024).
3. Y. Suzuki, T. Fujisawa, H. Sumikawa, T. Tanaka, C. Sugimoto, M. Kono, H. Hozumi, M. Karayama, K. Furuhashi, N. Enomoto, Y. Nakamura, N. Inui, T. Suda, Disease course and prognosis of pleuroparenchymal fibroelastosis compared with idiopathic pulmonary fibrosis. *Respir. Med.* **171**, 106078 (2020).
4. V. Cottin, S. Si-Mohamed, R. Diesler, P. Bonniaud, C. Valenzuela, Pleuroparenchymal fibroelastosis. *Curr. Opin. Pulm. Med.* **28**, 432–440 (2022).
5. P. Braubach, C. Werlein, S. E. Verleden, I. Maerzke, J. Gottlieb, G. Warnecke, S. Dettmer, F. Laenger, D. Jonigk, Pulmonary fibroelastotic remodelling revisited. *Cells* **10**, 1362 (2021).
6. N. Enomoto, H. Kusagaya, Y. Oyama, M. Kono, Y. Kaida, S. Kuroishi, D. Hashimoto, T. Fujisawa, K. Yokomura, N. Inui, Y. Nakamura, T. Suda, Quantitative analysis of lung elastic fibers in idiopathic pleuroparenchymal fibroelastosis (IPPFE): Comparison of clinical, radiological, and pathological findings with those of idiopathic pulmonary fibrosis (IPF). *BMC Pulm. Med.* **14**, 91 (2014).
7. E. Dann, A.-M. Cujba, A. J. Oliver, K. B. Meyer, S. A. Teichmann, J. C. Marioni, Precise identification of cell states altered in disease using healthy single-cell references. *Nat. Genet.* **55**, 1998–2008 (2023).
8. P. Ramachandran, R. Dobie, J. Wilson-Kanamori, E. Dora, B. Henderson, N. Luu, J. Portman, K. Matchett, M. Brice, J. Marwick, R. Taylor, M. Efremova, R. Vento-Tormo, N. Carragher, T. Kendall, J. Fallowfield, E. Harrison, D. Mole, S. Wigmore, P. Newsome, C. Weston, J. Iredale, F. Tacke, J. Pollard, C. Ponting, J. Marioni, S. Teichmann, N. Henderson, Resolving the fibrotic niche of human liver cirrhosis at single cell level. *Nature* **575**, 512–518 (2019).
9. A. M. A. Miranda, V. Janbandhu, H. Maatz, K. Kanemaru, J. Cranley, S. A. Teichmann, N. Hübner, M. D. Schneider, R. P. Harvey, M. Noseda, Single-cell transcriptomics for the assessment of cardiac disease. *Nat. Rev. Cardiol.* **20**, 289–308 (2023).
10. T. S. Adams, J. C. Schupp, S. Poli, E. A. Ayaub, N. Neumark, F. Ahangari, S. G. Chu, B. A. Raby, G. Deluliis, M. Januszyk, Q. Duan, H. A. Arnett, A. Siddiqui, G. R. Washko, R. Homer, X. Yan, I. O. Rosas, N. Kaminski, Single-cell RNA-seq reveals ectopic and aberrant lung-resident cell populations in idiopathic pulmonary fibrosis. *Sci. Adv.* **6**, eaba1983 (2020).
11. J. Obacz, J. A. Valer, R. Nibhani, T. S. Adams, J. C. Schupp, N. Veale, A. Lewis-Wade, J. Flint, J. Hogan, G. Aresu, A. S. Coonar, A. Peryt, G. Biffi, N. Kaminski, H. Francies, D. M. Rassl, M. J. Garnett, R. C. Rintoul, S. J. Marciniak, Single-cell transcriptomic analysis of human pleura reveals stromal heterogeneity and informs in vitro models of mesothelioma. *Eur. Respir. J.* **63**, 2300143 (2024).
12. M. Sauler, J. E. McDonough, T. S. Adams, N. Kothapalli, T. Barnthaler, R. B. Werder, J. C. Schupp, J. Nouws, M. J. Robertson, C. Coarfa, T. Yang, M. Chioccioli, N. Omote, C. Cosme Jr., S. Poli, E. A. Ayaub, S. G. Chu, K. H. Jensen, J. L. Gomez, C. J. Britto, M. S. B. Raredon, L. E. Niklason, A. A. Wilson, P. N. Timshel, N. Kaminski, I. O. Rosas, Characterization of the COPD alveolar niche using single-cell RNA sequencing. *Nat. Commun.* **13**, 494 (2022).
13. A. C. Habermann, A. J. Gutierrez, L. T. Bui, S. L. Yahn, N. I. Winters, C. L. Calvi, L. Peter, M. I. Chung, C. J. Taylor, C. Jetter, L. Raju, J. Roberson, G. Ding, L. Wood, J. M. S. Sucre,

B. W. Richmond, A. P. Serezani, W. J. McDonnell, S. B. Mallal, M. J. Bacchetta, J. E. Loyd, C. M. Shaver, L. B. Ware, R. Bremner, R. Walia, T. S. Blackwell, N. E. Banovich, J. A. Kropski, Single-cell RNA sequencing reveals profibrotic roles of distinct epithelial and mesenchymal lineages in pulmonary fibrosis. *Sci. Adv.* **6**, eaba1972 (2020).
14. A. Y. Zhao, A. Unterman, N. S. Abu Hussein, P. Sharma, F. Nekola, J. Flint, X. Yan, T. S. Adams, A. Justet, T. S. Sumida, J. Zhao, J. C. Schupp, M. S. B. Raredon, F. Ahangari, G. Deluliis, Y. Zhang, I. Buendia-Roldan, A. Adegunsoye, A. I. Sperling, A. Prasse, C. Ryu, E. Herzog, M. Selman, A. Pardo, N. Kaminski, Single-cell analysis reveals novel immune perturbations in fibrotic hypersensitivity pneumonitis. *Am. J. Respir. Crit. Care Med.* **210**, 1252–1266 (2024).
15. G. Raghu, M. Remy-Jardin, L. Richeldi, C. C. Thomson, Y. Inoue, T. Johkoh, M. Kreuter, D. A. Lynch, T. M. Maher, F. J. Martinez, M. Molina-Molina, J. L. Myers, A. G. Nicholson, C. J. Ryerson, M. E. Strek, L. K. Troy, M. Wijsenbeek, M. J. Mammen, T. Hossain, B. D. Bissell, D. D. Herman, S. M. Hon, F. Kheir, Y. H. Khor, M. Macrea, K. M. Antoniou, D. Bouros, I. Buendia-Roldan, F. Caro, B. Crestani, L. Ho, J. Morisset, A. L. Olson, A. Podolanczuk, V. Poletti, M. Selman, T. Ewing, S. Jones, S. L. Knight, M. Ghazipura, K. C. Wilson, Idiopathic pulmonary fibrosis (an update) and progressive pulmonary fibrosis in adults: An official ATS/ERS/JRS/ALAT clinical practice guideline. *Am. J. Respir. Crit. Care Med.* **205**, e18–e47 (2022).
16. D. J. Lederer, F. J. Martinez, Idiopathic pulmonary fibrosis. *N. Engl. J. Med.* **378**, 1811–1823 (2018).
17. D. A. Lynch, N. Sverzellati, W. D. Travis, K. K. Brown, T. V. Colby, J. R. Galvin, J. G. Goldin, D. M. Hansell, Y. Inoue, T. Johkoh, A. G. Nicholson, S. L. Knight, S. Raoof, L. Richeldi, C. J. Ryerson, J. H. Ryu, A. U. Wells, Diagnostic criteria for idiopathic pulmonary fibrosis: A Fleischner Society White Paper. *Lancet Respir. Med.* **6**, 138–153 (2018).
18. E. Gudmundsson, A. Zhao, N. Mogulkoc, I. Stewart, M. G. Jones, C. H. M. Van Moorsel, R. Savas, C. J. Brereton, H. W. Van Es, O. Unat, K. Pontoppidan, F. Van Beek, M. Veltkamp, B. Gholipour, A. Nair, A. U. Wells, S. M. Janes, D. C. Alexander, J. Jacob, Pleuroparenchymal fibroelastosis in idiopathic pulmonary fibrosis: Survival analysis using visual and computer-based computed tomography assessment. *EClinicalMedicine* **38**, 101009 (2021).
19. T. S. Adams, J. C. Schupp, A. Balayev, J. Khoury, A. Justet, F. Nikola, L. J. De Sadeleer, J. Cala-Garcia, M. Zapata-Ortega, P. V. Benos, J. E. McDonough, F. Ahangari, M. Königshoff, J. Ding, R. J. Homer, I. Rosas, X. Yan, B. M. Vanaudenaerde, W. A. Wuyts, N. Kaminski, Alveolar epithelial cell plasticity and injury memory in human pulmonary fibrosis. bioRxiv 2025.06.10.658504 [Preprint] (2025). https://doi.org/10.1101/2025.06.10.658504.
20. The Human Organ Atlas Collaboration, A. Bellier, A. Yendiki, B. De Bakker, C. Walsh, D. Jonigk, D. Stansby, G. Gaisne, H. Dejea I Velardo, J. Purzycka, J. Brunet, J. Jacob, M. Ackermann, P. Tafforeau, P. Lee, S. Verleden, T. Urban, Zoom (VOI-02) at 2.0um of the lung of donor A129, scanned at ESRF on beamline BM18, version 1, European Synchrotron Radiation Facility (2025); https://doi.org/10.15151/ESRF-DC-2184066672.
21. L. Richeldi, A. Azuma, V. Cottin, M. Kreuter, T. M. Maher, F. J. Martinez, J. M. Oldham, C. Valenzuela, E. Clerisme-Beaty, M. Gordat, D. Wachtlin, Y. Liu, C. Schlecker, S. Stowasser, D. F. Zoz, M. S. Wijsenbeek, Nerandomilast in patients with idiopathic pulmonary fibrosis. *N. Engl. J. Med.* **392**, 2193–2202 (2025).
22. L. Richeldi, R. M. D. Bois, G. Raghu, A. Azuma, K. K. Brown, U. Costabel, V. Cottin, K. R. Flaherty, D. M. Hansell, Y. Inoue, D. S. Kim, M. Kolb, A. G. Nicholson, P. W. Noble, M. Selman, H. Taniguchi, M. Brun, F. L. Maulf, M. Girard, S. Stowasser, R. Schlenker-Herceg, B. Disse, H. R. Collard, Efficacy and safety of nintedanib in idiopathic pulmonary fibrosis. *N. Engl. J. Med.* **370**, 2071–2082 (2014).
23. A. Vannan, R. Lyu, A. L. Williams, N. M. Negretti, E. D. Mee, J. Hirsh, S. Hirsh, N. Hadad, D. S. Nichols, C. L. Calvi, C. J. Taylor, V. Vasiliy, A. P. M. Polosukhin, A. S. Serezani, J. J. McCall, H. Gokey, L. B. Shim, M. J. Ware, C. M. Bacchetta, T. S. Shaver, R. Blackwell, J. M. S. Walia, J. A. Sucre, D. J. Kropski, N. E. McCarthy, Spatial transcriptomics identifies molecular niche dysregulation associated with distal lung remodeling in pulmonary fibrosis. *Nat. Genet.* **57**, 647–658 (2025).
24. X. Shao, I. N. Taha, K. R. Clauser, Y. T. Gao, A. Naba, MatrisomeDB: The ECM-protein knowledge database. *Nucleic Acids Res.* **48**, D1136–D1144 (2020).
25. C. H. Mayr, A. Sengupta, S. Asgharpour, M. Ansari, J. C. Pestoni, P. Ogar, I. Angelidis, A. Liontos, J. A. Rodriguez-Castillo, N. J. Lang, M. Strunz, D. Porras-Gonzalez, M. Gerckens, L. J. De Sadeleer, B. Oehrle, V. Viteri-Alvarez, I. E. Fernandez, M. Tallquist, M. Irmler, J. Beckers, O. Eickelberg, G. M. Stoleriu, J. Behr, N. Kneidinger, W. A. Wuyts, R. M. Wasnick, A. Ö. Yildirim, K. Ahlbrecht, R. E. Morty, C. Samakovlis, F. J. Theis, G. Burgstaller, H. B. Schiller, Sfrp1 inhibits lung fibroblast invasion during transition to injury-induced myofibroblasts. *Eur. Respir. J.* **63**, 2301326 (2024).
26. Y. Fang, S. S. W. Chung, L. Xu, C. Xue, X. Liu, D. Jiang, R. Li, Y. Korogi, K. Yuan, A. Saqi, H. Hibshoosh, Y. Huang, C.-S. Lin, T. Tsukui, D. Sheppard, X. Sun, J. Que, RUNX2 promotes fibrosis via an alveolar-to-pathological fibroblast transition. *Nature* **640**, 221–230 (2025).
27. T. Tsukui, P. J. Wolters, D. Sheppard, Alveolar fibroblast lineage orchestrates lung inflammation and fibrosis. *Nature* **631**, 627–634 (2024).
28. T. Tsukui, D. Sheppard, Stromal heterogeneity in the adult lung delineated by single-cell genomics. *Am. J. Physiol. Cell Physiol.* **328**, C1964–C1972 (2025).
29. C. Gago da Graça, L. G. M. van Baarsen, R. E. Mebius, Tertiary lymphoid structures: Diversity in their development, composition, and role. *J. Immunol.* **206**, 273–281 (2021).
30. T. N. Schumacher, D. S. Thommen, Tertiary lymphoid structures in cancer. *Science* **375**, eabf9419 (2022).
31. H. Fleige, S. Ravens, G. L. Moschovakis, J. Bölter, S. Willenzon, G. Sutter, S. Häussler, U. Kalinke, I. Prinz, R. Förster, IL-17-induced CXCL12 recruits B cells and induces follicle formation in BALT in the absence of differentiated FDCs. *J. Exp. Med.* **211**, 643–651 (2014).
32. Y. Liu, A. Sinjab, J. Min, G. Han, F. Paradiso, Y. Zhang, R. Wang, G. Pei, Y. Dai, Y. Liu, K. S. Cho, E. Dai, A. Basi, J. K. Burks, K. I. Rajapakshe, Y. Chu, J. Jiang, D. Zhang, X. Yan, P. A. Guerrero, A. Serrano, M. Li, T. H. Hwang, A. Futreal, J. A. Ajani, L. M. Solis Soto, A. A. Jazaeri, H. Kadara, A. Maitra, L. Wang, Conserved spatial subtypes and cellular neighborhoods of cancer-associated fibroblasts revealed by single-cell spatial multi-omics. *Cancer Cell* **43**, 905–924.e6 (2025).
33. M. G. Jones, A. Fabre, P. Schneider, F. Cinetto, G. Sgalla, M. Mavrogordato, S. Jogai, A. Alzetani, B. G. Marshall, K. M. A. O'Reilly, J. A. Warner, P. M. Lackie, D. E. Davies, D. M. Hansell, A. G. Nicholson, I. Sinclair, K. K. Brown, L. Richeldi, Three-dimensional characterization of fibroblast foci in idiopathic pulmonary fibrosis. *JCI Insight* **1**, e86375 (2016).
34. C. D. Cool, S. D. Groshong, P. R. Rai, P. M. Henson, J. S. Stewart, K. K. Brown, Fibroblast foci are not discrete sites of lung injury or repair: The fibroblast reticulum. *Am. J. Respir. Crit. Care Med.* **174**, 654–658 (2006).
35. L. Franzén, M. Olsson Lindvall, M. Hühn, V. Ptasinski, L. Setyo, B. P. Keith, A. Collin, S. Oag, T. Volckaert, A. Borde, J. Lundeberg, J. Lindgren, G. Belfield, S. Jackson, A. Ollerstam, M. Stamou, P. L. Ståhl, J. J. Hornberg, Mapping spatially resolved transcriptomes in human and mouse pulmonary fibrosis. *Nat. Genet.* **56**, 1725–1736 (2024).
36. C. H. Mayr, D. Santacruz, S. Jarosch, M. Bleck, J. Dalton, A. McNabola, C. Lempp, L. Neubert, B. Rath, J. C. Kamp, D. Jonigk, M. Kühnel, H. Schlüter, A. Klimowicz, J. Doerr, A. Dick, F. Ramirez, M. J. Thomas, Spatial transcriptomic characterization of pathologic niches in IPF. *Sci. Adv.* **10**, eadl5473 (2024).
37. J. Schipke, S. Panpeng, C. Wrede, J. Hegermann, J. Ruwisch, C. Werlein, D. Jonigk, H. Shin, J. Schupp, C. Mühlfeld, L. Knudsen, On the ultrastructure of aberrant basaloid cells in idiopathic pulmonary fibrosis. *Am. J. Respir. Cell Mol. Biol.* **71**, 746–750 (2024).
38. J. C. Schupp, T. S. Adams, C. Cosme Jr., M. S. B. Raredon, Y. Yuan, N. Omote, S. Poli, M. Chioccioli, K.-A. Rose, E. P. Manning, M. Sauler, G. Deluliis, F. Ahangari, N. Neumark, A. C. Habermann, A. J. Gutierrez, L. T. Bui, R. Lafyatis, R. W. Pierce, K. B. Meyer, M. C. Nawijn, S. A. Teichmann, N. E. Banovich, J. A. Kropski, L. E. Niklason, D. Pe'er, X. Yan, R. J. Homer, I. O. Rosas, N. Kaminski, Integrated single-cell atlas of endothelial cells of the human lung. *Circulation* **144**, 286–302 (2021).
39. J. C. Schupp, E. P. Manning, M. Chioccioli, J. C. Kamp, L. Christian, C. Ryu, E. Herzog, M. P. Kühnel, A. Prasse, N. Kaminski, D. D. Jonigk, R. J. Homer, Yale-MHH-MGH-Study Group, Alveolar vascular remodeling in nonspecific interstitial pneumonia: Replacement of normal lung capillaries with COL15A1 positive endothelial cells. *Am. J. Respir. Crit. Care Med.* **208**, 819–822 (2023).
40. L. M. Leiber, L. Christian, L. Neubert, J. Ruwisch, H. Yilmaz, E. K. J. Plucinski, L. Langer, J. C. Kamp, M. Greer, B. Haermeyer, M. Kühnel, C. Werlein, A. Justet, A. K. Bergmann, M. Ballmaier, J. Salman, L. Knudsen, U. Martin, B. Vanaudenaerde, A. Ö. Yildirim, F. Ius, F. Laenger, T. Welte, C. Falk, N. Kaminski, D. D. Jonigk, J. Gottlieb, J. C. Schupp, Aberrant and ectopic cell populations of the fibrotic pushing border in restrictive allograft syndrome after lung transplantation. bioRxiv 2024.06.04.597358 [Preprint] (2024). https://doi.org/10.1101/2024.06.04.597358.
41. V. Liakouli, A. Ciancio, F. Del Galdo, R. Giacomelli, F. Ciccia, Systemic sclerosis interstitial lung disease: Unmet needs and potential solutions. *Nat. Rev. Rheumatol.* **20**, 21–32 (2024).
42. E. Valenzi, M. Bulik, T. Tabib, C. Morse, J. Sembrat, H. Trejo Bittar, M. Rojas, R. Lafyatis, Single-cell analysis reveals fibroblast heterogeneity and myofibroblasts in systemic sclerosis-associated interstitial lung disease. *Ann. Rheum. Dis.* **78**, 1379–1387 (2019).
43. T. Flament, A. Bigot, B. Chaigne, H. Henique, E. Diot, S. Marchand-Adam, Pulmonary manifestations of Sjögren's syndrome. *Eur. Respir. Rev.* **25**, 110–123 (2016).
44. G. Leuschner, A. Semenova, C. H. Mayr, T. S. Kapellos, M. Ansari, B. Seeliger, M. Frankenberger, N. Kneidinger, R. A. Hatz, A. Hilgendorff, A. Prasse, J. Behr, M. Mann, H. B. Schiller, Mass spectrometry-based autoimmune profiling reveals predictive autoantigens in idiopathic pulmonary fibrosis. *iScience* **26**, 108345 (2023).
45. A. Unterman, A. Y. Zhao, N. Neumark, J. C. Schupp, F. Ahangari, C. Cosme Jr., P. Sharma, J. Flint, Y. Stein, C. Ryu, G. Ishikawa, T. S. Sumida, J. L. Gomez, J. D. Herazo-Maya, C. S. Dela, Cruz, E. L. Herzog, N. Kaminski, Single-cell profiling reveals immune aberrations in progressive idiopathic pulmonary fibrosis. *Am. J. Respir. Crit. Care Med.* **210**, 484–496 (2024).
46. G. Raghu, K. J. Anstrom, T. E. King, J. A. Lasky, F. J. Martinez, Prednisone, azathioprine, and N-acetylcysteine for pulmonary fibrosis. *N. Engl. J. Med.* **366**, 1968–1977 (2012).
47. C. A. Newton, D. Zhang, J. M. Oldham, J. Kozlitina, S.-F. Ma, F. J. Martinez, G. Raghu, I. Noth, C. K. Garcia, Telomere length and use of immunosuppressive medications in idiopathic pulmonary fibrosis. *Am. J. Respir. Crit. Care Med.* **200**, 336–347 (2019).

48. R. Borie, D. Bouvry, V. Cottin, C. Gauvain, A. Cazes, M.-P. Debray, J. Cadranel, P. Dieude, T. Degot, S. Dominique, A. S. Gamez, M. Jaillet, P.-A. Juge, A. Londono-Vallejo, A. Mailleux, H. Mal, C. Boileau, C. Menard, H. Nunes, G. Prevot, S. Quetant, P. Revy, J. Traclet, L. Wemeau-Stervinou, M. Wislez, C. Kannengiesser, B. Crestani, Regulator of telomere length 1 (RTEL1) mutations are associated with heterogeneous pulmonary and extra-pulmonary phenotypes. *Eur. Respir. J.* **53**, 1800508 (2019).
49. A. Adegunsoye, J. A. Kropski, J. Behr, T. S. Blackwell, T. J. Corte, V. Cottin, A. R. Glanville, M. K. Glassberg, M. Griese, G. M. Hunninghake, K. A. Johannson, M. P. Keane, J. S. Kim, M. Kolb, T. M. Maher, J. M. Oldham, A. J. Podolanczuk, I. O. Rosas, F. J. Martinez, I. Noth, D. A. Schwartz, Genetics and genomics of pulmonary fibrosis: Charting the molecular landscape and shaping precision medicine. *Am. J. Respir. Crit. Care Med.* **210**, 401–423 (2024).
50. T. Tabib, M. Huang, N. Morse, A. Papazoglou, R. Behera, M. Jia, M. Bulik, D. E. Monier, P. V. Benos, W. Chen, R. Domsic, R. Lafyatis, Myofibroblast transcriptome indicates SFRP2^{hi} fibroblast progenitors in systemic sclerosis skin. *Nat. Commun.* **12**, 4384 (2021).
51. M. Decker, L. Martinez-Morentin, G. Wang, Y. Lee, Q. Liu, J. Leslie, L. Ding, Leptin-receptor-expressing bone marrow stromal cells are myofibroblasts in primary myelofibrosis. *Nat. Cell Biol.* **19**, 677–688 (2017).
52. R. De Man, J. E. McDonough, T. S. Adams, F. Nikola, R. Rangel, S. Anderson, E. P. Manning, J. Cala Garcia, B. Moss, A. Waich, F. Poli, R. Cardenas, C. Coarfa, Q. Song, Z. Bar-Joseph, B. M. Vanaudenaerde, W. A. Wuyts, L. Niklason, M. S. B. Raredon, X. Yan, I. O. Rosas, N. Kaminski, Single-cell atlas of human lung aging identifies cell type dyssynchrony and increased transcriptional entropy. *Nat. Commun.* **17**, 2095 (2026).
53. L. Sikkema, C. Ramírez-Suástegui, D. C. Strobl, T. E. Gillett, L. Zappia, E. Madissoon, N. S. Markov, L.-E. Zaragosi, Y. Ji, M. Ansari, M.-J. Arguel, L. Apperloo, M. Banchero, C. Bécavin, M. Berg, E. Chichelnitskiy, M.-I. Chung, A. Collin, A. C. A. Gay, J. Gote-Schniering, B. H. Kashani, K. Inecik, M. Jain, T. S. Kapellos, T. M. Kole, S. Leroy, C. H. Mayr, A. J. Oliver, M. von Papen, L. Peter, C. J. Taylor, T. Walzthoeni, C. Xu, L. T. Bui, C. De Donno, L. Dony, A. Faiz, M. Guo, A. J. Gutierrez, L. Heumos, N. Huang, I. L. Ibarra, N. D. Jackson, P. K. L. Murthy, M. Lotfollahi, T. Tabib, C. Talavera-López, K. J. Travaglini, A. Wilbrey-Clark, K. B. Worlock, M. Yoshida, Lung Biological Network Consortium, M. van den Berge, Y. Bossé, T. J. Desai, O. Eickelberg, N. Kaminski, M. A. Krasnow, R. Lafyatis, M. Z. Nikolic, J. E. Powell, J. Rajagopal, M. Rojas, O. Rozenblatt-Rosen, M. A. Seibold, D. Sheppard, D. P. Shepherd, D. D. Sin, W. Timens, A. M. Tsankov, J. Whitsett, Y. Xu, N. E. Banovich, P. Barbry, T. E. Duong, C. S. Falk, K. B. Meyer, J. A. Kropski, D. Pe'er, H. B. Schiller, P. R. Tata, J. L. Schultze, S. A. Teichmann, A. V. Misharin, M. C. Nawijn, M. D. Luecken, F. J. Theis, An integrated cell atlas of the lung in health and disease. *Nat. Med.* **29**, 1563–1577 (2023).
54. C. Domínguez Conde, C. Xu, L. B. Jarvis, D. B. Rainbow, S. B. Wells, T. Gomes, S. K. Howlett, O. Suchanek, K. Polanski, H. W. King, L. Mamanova, N. Huang, P. A. Szabo, L. Richardson, L. Bolt, E. S. Fasouli, K. T. Mahbubani, M. Prete, L. Tuck, N. Richoz, Z. K. Tuong, L. Campos, H. S. Mousa, E. J. Needham, S. Pritchard, T. Li, R. Elmentaite, J. Park, E. Rahmani, D. Chen, D. K. Menon, O. A. Bayraktar, L. K. James, K. B. Meyer, N. Yosef, M. R. Clatworthy, P. A. Sims, D. L. Farber, K. Saeb-Parsy, J. L. Jones, S. A. Teichmann, Cross-tissue immune cell analysis reveals tissue-specific features in humans. *Science* **376**, eabl5197 (2022).
55. J. Brunet, C. L. Walsh, W. L. Wagner, A. Bellier, C. Werlein, S. Marussi, D. D. Jonigk, S. E. Verleden, M. Ackermann, P. D. Lee, P. Tafforeau, Preparation of large biological samples for high-resolution, hierarchical, synchrotron phase-contrast tomography with multimodal imaging compatibility. *Nat. Protoc.* **18**, 1441–1461 (2023).
56. J. Hegermann, C. Wrede, S. Fassbender, R. Schliep, M. Ochs, L. Knudsen, C. Mühlfeld, Volume-CLEM: A method for correlative light and electron microscopy in three dimensions. *Am. J. Physiol. Lung Cell. Mol. Physiol.* **317**, L778–L784 (2019).
57. P. Bankhead, M. B. Loughrey, J. A. Fernández, Y. Dombrowski, D. G. McArt, P. D. Dunne, S. McQuaid, R. T. Gray, L. J. Murray, H. G. Coleman, J. A. James, M. Salto-Tellez, P. W. Hamilton, QuPath: Open source software for digital pathology image analysis. *Sci. Rep.* **7**, 16878 (2017).
58. U. Schmidt, M. Weigert, C. Broaddus, G. Myers, Cell detection with star-convex polygons. arXiv:1806.03535 [cs.CV] (2018).
59. J. F. Ouyang, U. S. Kamaraj, E. Y. Cao, O. J. L. Rackham, ShinyCell: Simple and sharable visualization of single-cell gene expression data. *Bioinformatics* **37**, 3374–3376 (2021).
60. A. Butler, P. Hoffman, P. Smibert, E. Papalexi, R. Satija, Integrating single-cell transcriptomic data across different conditions, technologies, and species. *Nat. Biotechnol.* **36**, 411–420 (2018).
61. T. Tsukui, K. H. Sun, J. B. Wetter, J. R. Wilson-Kanamori, L. A. Hazelwood, N. C. Henderson, T. S. Adams, J. C. Schupp, S. D. Poli, I. O. Rosas, N. Kaminski, M. A. Matthay, P. J. Wolters, D. Sheppard, Collagen-producing lung cell atlas identifies multiple subsets with distinct localization and relevance to fibrosis. *Nat. Commun.* **11**, 1920 (2020).
62. D. Dimitrov, D. Türei, M. Garrido-Rodriguez, P. L. Burmedi, J. S. Nagai, C. Boys, R. O. Ramirez Flores, H. Kim, B. Szalai, I. G. Costa, A. Valdeolivas, A. Dugourd, J. Saez-Rodriguez, Comparison of methods and resources for cell-cell communication inference from single-cell RNA-Seq data. *Nat. Commun.* **13**, 3224 (2022).
63. R. Browaeys, J. Gilis, C. Sang-Aram, P. D. Bleser, L. Hoste, S. Tavernier, D. Lambrechts, R. Seurinck, Y. Saeys, MultiNicheNet: A flexible framework for differential cell-cell communication analysis from multi-sample multi-condition single-cell transcriptomics data. bioRxiv 2023.06.13.544751 [Preprint] (2023). https://doi.org/10.1101/2023.06.13.544751.
64. S. Jin, M. V. Plikus, Q. Nie, CellChat for systematic analysis of cell-cell communication from single-cell and spatially resolved transcriptomics. bioRxiv 2023.11.05.565674 [Preprint] (2023). https://doi.org/10.1101/2023.11.05.565674.
65. M. I. Love, W. Huber, S. Anders, Moderated estimation of fold change and dispersion for RNA-seq data with DESeq2. *Genome Biol.* **15**, 550 (2014).
66. G. Finak, A. McDavid, M. Yajima, J. Deng, V. Gersuk, A. K. Shalek, C. K. Slichter, H. W. Miller, M. J. McElrath, M. Prlic, P. S. Linsley, R. Gottardo, MAST: A flexible statistical framework for assessing transcriptional changes and characterizing heterogeneity in single-cell RNA sequencing data. *Genome Biol.* **16**, 278 (2015).
67. D. A. Barbie, P. Tamayo, J. S. Boehm, S. Y. Kim, S. E. Moody, I. F. Dunn, A. C. Schinzel, P. Sandy, E. Meylan, C. Scholl, S. Fröhling, E. M. Chan, M. L. Sos, K. Michel, C. Mermel, S. J. Silver, B. A. Weir, J. H. Reiling, Q. Sheng, P. B. Gupta, R. C. Wadlow, H. Le, S. Hoersch, B. S. Wittner, S. Ramaswamy, D. M. Livingston, D. M. Sabatini, M. Meyerson, R. K. Thomas, E. S. Lander, J. P. Mesirov, D. E. Root, D. G. Gilliland, T. Jacks, W. C. Hahn, Systematic RNA interference reveals that oncogenic KRAS-driven cancers require TBK1. *Nature* **462**, 108–112 (2009).

Acknowledgments: We are grateful to all patients and control subjects who participated in this study. Special thanks to L. Giercke from the Schupp Lab at Hannover Medical school for support with the IF and ISH imaging. We thank S. Fassbender and S. Kuhlmann of the institute of functional and applied anatomy for great expertise in TEM sample preparation. We also want to express our gratitude to R. Engelhardt and C. Petzold-Mügge from the Department of Pathology at Hannover Medical School for help and expertise in localizing and sectioning for the archived FFPE blocks. We are also thankful to the Fiedler and Braun research groups for providing laboratory equipment. J.J. was also supported by the NIHR UCLH Biomedical Research Centre. Part of this research was performed within the context of the INFIBREX consortium and has benefited from the support of the "France 2030" investment plan, implemented by Université Paris Cité under its "Initiative of Excellence" IdEx program (ANR-18-IDEX-0001). Illustrations in Figs. 1A, 3 (J, K, and N), 5A, 6 (H and J), 7 (A and J), and 9 and fig. S11 (G and H) were created in BioRender. Schupp, J. (2026) https://biorender.com/br8cgh6. **Funding:** This project was supported by the Else Kröner-Fresenius Foundation (2023_EKCS.18) to J.C.S.; German Center for Lung research (FKZ 82DZL002B1, FKZ 82DZL002C1, and FKZ 82DZLT82C1) to J.C.S; Fondation du Souffle (FR-2024) to A.J.; PRACTIS Clinician Scientist Program, funded by Hannover Medical School and DFG (DFG ME 3696/3) to J.R. and B.S.; GlaxoSmithKline, Wellcome Trust (209553/Z/17/Z and 227835/Z/23/Z), Microsoft Research, Gilead Sciences, and Chan Zuckerberg Initiative (CZIF2024-009938) to J.J.; and National Institutes of Health (NIH) grants and National Heart, Lung, and Blood Institute (NHLBI) grants R01HL127349, R01HL141852, U01HL145567, and UH2HL123886 to N.K. **Author contributions:** Conceptualization: J.R., R.B., W.A.W., A.P., J.B., E.F., D.J., J.G., H.S., N.K., A.J., and J.C.S. Data curation: J.R., A.S., J.F., M.B., M.A., J.G., H.M., D.J., S.D., P.M., W.A.W., A.J., and J.C.S. Formal analysis: J.R., J.F., J.J., M.G., M.A., D.J., W.A.W., A.J., and J.C.S. Funding acquisition: B.V. and J.C.S. Investigation: J.R., A.C., L.M.L., R.B., L.C., V.T.d.M., A.S., J.H., M.B., J.J., J.B., P.B., L.J.D.S., L.K., H.M., E.B., D.J., P.M., A.P., W.A.W., N.K., A.J., and J.C.S. Methodology: J.R., L.M.L., S.E.V., J.H., J.F., J.J., C.W., A.P., C.F., B.V., J.B., L.K., D.J., W.A.W., A.J., and J.C.S. Project administration: J.R., L.M.L., C.W., A.P., A.J., and J.C.S. Resources: A.C., R.B., L.N., V.T.d.M., A.S., S.E.V., M.B., J.C.K., J.J., P.B., L.J.D.S., M.G., C.W., T.G., M.A., J.G., B.V., B.S., M.-P.D., J.B., L.K., E.B., H.M., D.J., P.M., A.P, E.F., W.A.W., B.C., N.K., A.J., and J.C.S. Software: J.R., S.G., J.F., J.J., and J.C.S. Supervision: J.J., M.A., C.F., J.G., B.S., E.B., D.J., W.A.W., N.K., A.J., and J.C.S. Validation: J.R., L.M.L., V.T.d.M., F.M., M.B., M.G., C.W., F.I., T.G., K.A., M.A., J.G., B.V., D.J., W.A.W., A.J., and J.C.S. Visualization: J.R., A.C., L.M.L., R.B., V.T.d.M., A.S., S.E.V., J.F., J.J., K.A., R.E., M.A., D.Y., L.K., E.B., D.J., S.D., W.A.W., B.C., and A.J. Writing—original draft: J.R., S.E.V., M.A., D.J., A.J., and J.C.S. Writing—review and editing: J.R., A.C., L.M.L., R.B., L.N., A.S., S.E.V., S.G., J.F., M.B., J.C.K., J.J., M.G., P.B., C.W., F.I., T.G., K.A., L.J.D.S., R.E., M.A., D.Y., M.M.H., C.F., J.G., H.S., B.V., B.S., L.K., E.B., H.M., D.J., S.D., P.M., A.P., W.A.W., B.C., N.K., A.J., and J.C.S. **Competing interests:** J.R. has received lecturing fees and travel grants from Boehringer Ingelheim, CSL Behring, and AstraZeneca all not related to this work. B.S. received lecturing and consulting fees from Boehringer Ingelheim, GlaxoSmithKline, AstraZeneca, and Chiesi all not related to this work. N.K. reports consulting to Boehringer Ingelheim, Pliant, GSK, Three Lake Partners, Merck, AstraZeneca, RohBar, BMS, Galapagos, Chiesi, Sofinnova, and Fibrogen, equity in Pliant, and grants from AstraZeneca and BMS. N.K. has IP on novel biomarkers and therapeutics in IPF licensed to Biotech. J.J. declares consultancy fees from Boehringer Ingelheim, F. Hoffmann-La Roche, GlaxoSmithKline, and NHSX; fees from advisory boards for Boehringer Ingelheim and F. Hoffmann-La Roche; lecture fees from Boehringer Ingelheim, F. Hoffmann-La Roche, and Takeda; and grant funding from GlaxoSmithKline, Wellcome Trust, Microsoft Research, Gilead Sciences, and Chan Zuckerberg Initiative. M.M.H. has received fees for consultations or lectures from 35Pharma, Acceleron, Actelion, Aerovate, AOP Health, Bayer, Ferrer, Gossamer, Inhibikase, Janssen, Keros, MSD, and Novartis. R.B. has received fees for consultations, lectures, or travel from Boehringer Ingelheim, Ferrer, and Sanofi. S.E.V. declares

grants to institute from Genentech, Chiesi, and AstraZeneca. M.-P.D. has received fees for consultations, lectures, or travel from Boehringer Ingelheim, Sanofi, and Bracco. C.W. received speaker fees from Boehringer Ingelheim. B.C. received honoraria for speaking or consulting, or travel grants, from Abbvie, AstraZeneca, BMS, Boehringer Ingelheim, Chiesi, CSL Behring, Glycocore, GSK, Menarini, MSD, Roche, and Sanofi. J.C.S. served as a consultant to Boehringer Ingelheim, Merck/MSD, GSK, AOP Health, Vicore Pharma, and Insmed and received lecture honoraria from Boehringer Ingelheim, GSK, and Kinevant. J.C.S. and A.P. have IP on basal cell-targeted therapies in IPF. A.J. reports consulting from Boehringer Ingelheim, Sanofi Regeneron, and AstraZeneca. The other authors declare that they have no competing interests. **Data, code, and materials availability:** All data and code needed to evaluate and reproduce the results in the paper are present in the paper and/or the Supplementary Materials. Raw snRNA-seq sequencing data de novo generated in this study were deposited on Gene Expression Omnibus under GSE301982 (https://ncbi.nlm.nih.gov/geo/query/acc.cgi?acc=GSE301982). Raw datasets from seven additional CTRL samples (GSE284081; https://ncbi.nlm.nih.gov/geo/query/acc.cgi?acc=GSE284081) and nine IPF samples (GSE286182; https://ncbi.nlm.nih.gov/geo/query/acc.cgi?acc=GSE286182) are also available on the Gene Expression Omnibus. The entire processed and integrated PPFE atlas dataset can be explored on the PPFE atlas web page (landing page: https://PPFEatlas.com, Epithelium: https://breath.mh-hannover.de/PPFE_Atlas/Epithel/, Mesenchyme: https://breath.mh-hannover.de/PPFE_Atlas/Mesenchym/, Endothelium: https://breath.mh-hannover.de/PPFE_Atlas/Endothel/, Myeloid: https://breath.mh-hannover.de/PPFE_Atlas/Myeloid/, and Lymphoid: https://breath.mh-hannover.de/PPFE_Atlas/Lymphoid/). Custom code used for analyses is available at Zenodo (https://doi.org/10.5281/zenodo.18891887) and GitHub (https://github.com/Ruwischj/ThePPFEatlas.git). No new materials were generated in this study.

Submitted 19 August 2025
Accepted 2 April 2026
Published 8 May 2026
10.1126/sciadv.aeb5967

ScienceAdvances

The pleuroparenchymal fibroelastosis atlas reveals aberrant cell states and their zonation as an alternate roadmap to lung fibrosis

Jannik Ruwisch, Aurélie Cazes, Lena M. Leiber, Raphaël Borie, Lavinia Neubert, Leonard Christian, Vincent Thomas de Montpréville, Adam Szmul, Farah Moussa, Stijn E. Verleden, Svenja Gaedcke, Jan Hegermann, Jan Fuge, Matthias Ballmaier, Jan C. Kamp, Mark Greer, Peter Braubach, Christopher Werlein, Fabius Ius, Theresa Graalmann, Kalil Aburahma, Laurens J. De Sadeleer, Ryoko Egashira, Maximilian Ackermann, Daisuke Yamada, Marius M. Hoeper, Christine Falk, Jens Gottlieb, Herbert B. Schiller, Bart Vanaudenaerde, Benjamin Seeliger, Marie-Pierre Debray, Jean Francois Bernaudin, Lars Knudsen, Emmanuel Bergot, Joseph Jacob, Hervé Mal, Danny Jonigk, Sabine Dettmer, Pierre Mordant, Antje Prasse, Elie Fadel, Wim A. Wuyts, Bruno Crestani, Naftali Kaminski, Aurélien Justet, and Jonas C. Schupp

Sci. Adv. **12** (19), eaeb5967. DOI: 10.1126/sciadv.aeb5967

Science Advances (ISSN 2375-2548) is published by the American Association for the Advancement of Science. 1200 New York Avenue NW, Washington, DC 20005. The title *Science Advances* is a registered trademark of AAAS.